# Local Inhibitory Dynamics Underpin Temporal Integration and Functional Segregation between Barrels and Septa in the Mouse Barrel Cortex

Ali Özgür Argunşah[1,2], Tevye Jason Stachniak[1,2,3], Jenq-Wei Yang[1,2], Linbi Cai[1,2], Alexander van der Bourg[1,2], Rahel Kastli[1,2,4], Theofanis Karayannis[1,2,5,*]

[1]Laboratory of Neural Circuit Assembly, Brain Research Institute, University of Zurich Winterthurerstrasse 190, CH-8057 Zurich, Switzerland.

[2]Neuroscience Center Zurich, University of Zurich and ETH Zurich, Winterthurerstrasse 190, CH-8057 Zurich, Switzerland.

[3]Division of Biomedical Sciences, Faculty of Medicine, Memorial University of Newfoundland, St. John's, A1B 3V6, Canada.

[4]Department of Stem Cell & Regenerative Biology, Harvard University, Cambridge, MA, USA.

[5]University Research Priority Program (URPP), Adaptive Brain Circuits in Development and Learning, University of Zurich, Zurich, Switzerland.

[*]Correspondence: karayannis@hifo.uzh.ch

**Abstract**

Just as separated digits and repeated sampling enhance somatosensation in humans, mice sense objects through multiple segregated whiskers through successive contacts. Individual whisker identity is maintained through the somatotopic organization of the Whisker→Brainstem→Thalamus→Cortex axis, culminating in distinct cortical domains: barrels and the surrounding septa. By performing simultaneous recordings using in-vivo electrophysiology in wild-type (WT) mice, we identify a progressive divergence in spiking activity between these domains upon repeated behaviorally relevant (10Hz) single- and multi-whisker stimulation. While the spiking activity ratio of multi- to single-whisker stimulation remains stable in barrels, it increases progressively in septa, suggesting inhibitory cell recruitment. Using genetic fate-mapping and tissue clearing, we indeed reveal that SST+ and VIP+ interneurons exhibit distinct laminar and regional distributions in barrel and septa domains. Further, calcium imaging of SST+ and VIP+ interneurons

shows that while both neuron types respond to single-whisker stimulus, SST+ interneurons preferentially engage more in 10Hz multi-whisker stimulation, indicating their critical role in progressive stimulus preference. Genetic removal of Elfn1, which regulates the incoming excitatory synaptic dynamics onto SST+ interneurons, leads to the loss of the progressive increase in septal spiking activity upon multi-whisker stimulation, resembling the stable response pattern observed in barrels. The importance of the loss of functional segregation of barrels, versus septa is revealed by cumulative temporal decoding analysis, supporting the notion that SST+ interneuron-mediated inhibition contributes to temporal encoding and stimulus integration. Finally, viral tracing combined with whole brain clearing and imaging reveals that barrel and septa domains project differentially to secondary somatosensory (S2) and motor (M1) cortices. These distinct projection patterns suggest that differential inhibitory processing in barrels and septa may contribute to functionally specialized downstream signaling. Together, our findings indicate that the progressive engagement of SST+ interneurons, mediated by Elfn1-dependent synaptic facilitation, underlies the preferential integration of multi-whisker stimuli in septa. This local inhibitory mechanism likely contributes to the functional segregation of barrel and septa domains and their distinct cortical projections, shaping how sensory information is processed and relayed to higher-order brain regions.

**Keywords**

Barrel Cortex, Elfn1 Knockout, Somatosensory Whisker Coding, Cortical Domains, Temporal Dynamics, Synaptic Integration, Sensory Projections, Network Segregation

## Introduction

Although the somatosensory whisker system is one of the principal means by which mice sense their environment and navigate the world, these tasks are carried out by a relatively small number of whiskers. This small number of vibrissae is represented in the whisker somatosensory cortex as barrel “islands” (columns) separated and surrounded by the septal “sea” (compartments), reminiscent of the whisker pad pattern on a rodent’s face, where sparse hair follicles are separated by spaces between them. In contrast, other sensory systems, such as the auditory and the visual ones, have densely packed

anatomical receptor configurations and cortical representations. Although all sensory cortices are composed of canonical microcircuits (Douglas and Martin, 2004) that include similar populations of excitatory and inhibitory neurons, maintaining segregated individual whisker information may require anatomical specializations, the barrel and septa domains. These domains may therefore create a distinct spatiotemporal stimulus representation and information coding in the barrel cortex, different from the other sensory modalities. In the adult murine barrel cortex, thalamocortical inputs coming from the ventro-postero-medial (VPM) and postero-medial (PoM) nuclei segregate into the barrel and septa domains, respectively (Alloway, 2008; Bureau et al., 2006; Kim and Ebner, 1999; Staiger and Petersen, 2021). Further, in mice (Audette et al., 2018; Sato and Svoboda, 2010; Shepherd and Svoboda, 2005) and rats (Alloway, 2008; Chakrabarti and Alloway, 2006; Melzer et al., 2006b) it was shown that information processing and flow within and from these domains target anatomically distinct sensory and motor areas. It has been suggested that the primary whisker somatosensory cortex (wS1) sends higher dimensional information needed for object recognition to the secondary somatosensory cortex (wS2), while the projections to the primary motor cortex (M1) carry less complex information that does not require segregated streams of information coming from individual whiskers (Alloway, 2008; Brecht and Sakmann, 2002; Cai et al., 2022; Sato and Svoboda, 2010). This divergence in information processing is also found within the barrel- and septa-related circuits. While barrel circuits are more involved in processing spatiotemporal whisker-object interactions, the septal circuits are more sensitive to the frequency of whisker movements, which suggests the use of temporal versus rate coding of information in barrel and septa, respectively (Melzer et al., 2006a, 2006b). Hence the existence of the septal column separating the barrels may provide mice with the means to separate these two interconnected yet very distinct information-processing routes along the temporal domain, and to make sense of their somatosensory environment through repeated sampling via cloistered information streams. Recent studies in mice have shown that barrel and septa compartments are not only anatomically segregated in terms of cell-type specific thalamocortical projections and differential expression of different genetic markers (Young et al., 2023) but also in their tuning upon single- and multi- whisker stimulation (Wang et al. 2022).

In both rats and mice, the operational identity of barrels and septa has often been attributed to the parallel bottom-up thalamocortical pathways of VPM and PoM. Here, by performing *in-vivo* silicon probe recordings simultaneously in the barrel and septa domains upon repeated single- and multi- whisker stimulation in wS1 of mice, we first show and characterize the temporal divergence between these domains. Utilizing genetic fate-mapping, passive tissue clearing, and light-sheet microscopy, we reveal that cortical somatostatin (SST+) and vasoactive intestinal peptide (VIP+) expressing interneurons show a layer-dependent differential distribution in the barrel versus septa columns. Through two-photon calcium imaging of these two populations, we show a differential engagement of SST+ cells upon multi- vs. single-whisker stimulation. By altering the short-term synaptic dynamics of incoming excitation onto these interneurons through the removal of the trans-synaptic protein Elfn1 (Elfn1 KO), we find that the column-specific contrast ratio between multi- over single- whisker response to a repetitive stimulus is diminished. Through a progressive decoding analysis, we find that in contrast to control, whisker stimulation-evoked Elfn1 KO responses in different domains cannot be decoded efficiently. Finally, using *in-vivo* retrograde viral-based tracing, we show a layer-specific projection preference between these domains and downstream regions wS2 and M1. Hence, in addition to the anatomical specialization through thalamocortical pathways, we reveal a key contribution of local lateral cortical inhibition, provided by SST+ interneurons, in setting up the functional segregation of barrel and septa domains, and subsequently, their downstream targets.

## Results

### Barrel and Septa columns display differentially adaptive spiking upon repeated single- and multi- whisker stimulation

To characterize the temporal stimulus-response profiles of barrel and septal domains simultaneously, we performed *in-vivo* multi-shank (8x8) silicon probe recordings under urethane-induced light anesthesia from mouse somatosensory whisker barrel cortex (wS1), after the age of active whisking onset, postnatal day (P)20-30. Whisker stimulation was performed on either just one principal whisker (single-whisker stimulus or SWS) or via both the principal whisker and most of the macro vibrissae together (multi-whisker

stimulus or MWS; see methods) (Figure 1A). Single- or multi- whisker evoked activity within identified regions was recorded upon a 2s-long stimulation at 10Hz, similar to the average frequency at which mice actively whisk (Carvell and Simons, 1990; Grant et al., 2012). Each mouse received both stimulation paradigms. Current source density (CSD) analysis was used to assess the location of each silicon probe shank, which was later verified by post-hoc histology. The recorded activity was assigned to the stimulated principal barrel column (B), the adjacent septal column (S), or the adjacent unstimulated neighboring barrel column (N) according to SWS paradigm (Figure 1B and Supp Figure 1A to D). An example probe assignment can be seen in Supp Figure 1E. While this distinctive experimental paradigm is relatively low throughput, it has allowed us to investigate all three of these domains simultaneously. The septal compartments in mouse barrel cortex are quite narrow (Bureau et al., 2006; Sato et al., 2007) and there is the possibility of rotational misalignment during the insertion of silicon probes into the brain (Supp. Figure 1F). For these reasons we restricted our analysis of *in-vivo* responses upon SWS and MWS between barrel and septa responses to upper layers and L4, for which we have higher confidence about the anatomical domain allocation after our histological (Supp. Figure 1B) and CSD analysis (Supp. Figure 1C and D). In line with this domain allocation, t-distributed stochastic neighbor embedding (t-SNE) analysis of the multi-unit activity (MUA) recorded across the entire train of stimuli in the different domains revealed that the spiking responses between the principal barrel and the neighboring one form two separate clusters, while the responses recorded in the septa lay in between (Figure 1C; see methods).

It has previously been shown that electrophysiological responses upon whisking-based object detection saturate rapidly after a single whisker touch, while object localization may require multiple repeated whisker touches (O'Connor et al., 2013; Pammer et al., 2013). Correspondingly, when a single whisker is stimulated repeatedly, the response to the first pulse is principally bottom-up thalamic-driven responses, while the later pulses in the train are expected to also gradually engage cortico-thalamo-cortical and cortico-cortical loops. We therefore first tested whether the leading pulses of the stimulus train evoked differential responses among the principal barrel, the adjacent septa, and the neighboring barrel upon SWS and MWS. For easier visualization and full appreciation of the data, we

157 present our findings both in classical time series firing-rate plot and stimulation pulse
158 aligned stacked images (Supp. Figure 2A and B, 200ms baseline followed by 2000ms
159 evoked response to 20 pulses at 10Hz reshaped to 20 stacked 100ms-long evoked
160 response image, left to right). Earlier studies that separately recorded whisker-evoked
161 responses from either barrel or septa domains in rat reported that the responses of barrel
162 neurons to single principal whisker stimulation are much higher than those evoked in the
163 septal neurons (Armstrong-James and Fox, 1987; Brecht and Sakmann, 2002). The
164 analysis of the data we obtained from the simultaneous recordings at these domains in
165 the mouse do not reveal such differences in the first two stimulus responses in L4 upon
166 single whisker stimulation (SWS) (Figure 1D; statistics on the bottom; white represents
167 no significance). However, response differences emerged from the 3$^{rd}$ pulse onward upon
168 SWS (Figure 1D, bottom). Similar differences also emerged between stimulated principal
169 and unstimulated neighboring barrel columns upon SWS (starting from 4$^{th}$ pulse,
170 Figure1D, bottom, Barrel-vs-Neighbor (BN) row). Interestingly, an inverted pattern of
171 significance appeared between septa and adjacent unstimulated neighboring barrels
172 (Figure 1D, bottom, Septa-vs-Neighbor (SN) row). When multiple whiskers (MWS) were
173 activated simultaneously, like SWS, a divergence between barrel and septa domain
174 activity also occurred in Layer 4 from the 2$^{nd}$ pulse onward (Figure 1E). Finally, when we
175 calculated the response ratio upon MW over SW stimulation, we saw that the septal
176 MW/SW ratio diverged from barrel MW/SW ratio over the course of repeated stimulation
177 (Figure 1F), indicating a role of septal neurons in the progressive processing MW
178 information.
179
180 **Barrel and Septa columns display differential SST+ and VIP+ neuron densities**
181 It is known that barrel and septa domains receive different thalamic projections, from VPM
182 and PoM respectively, that might affect stimulus response properties (Ahissar et al., 2001;
183 Chmielowska et al., 1989; Koralek et al., 1988; Sosnik et al., 2001). Our
184 electrophysiological experiments show a significant divergence of responses over time
185 upon both SWS and MWS in L4 between barrels (principal and neighboring) and adjacent
186 septa, with minimal initial difference. We hypothesized that this late divergence might be
187 driven by differences in the local circuitry, and specifically inhibitory cells. We therefore

188 next assessed the spatial distribution of two inhibitory cell populations that could provide
189 distinct regulation of cortical activity in the temporal domain: SST+ and VIP+ cells.
190 Earlier research examining the three largest inhibitory neuron populations in the mouse
191 barrel cortex showed that, while parvalbumin positive (PV+) cells do not show any
192 differential density preference between barrel and septa columns, SST+ and VIP+ cells
193 have higher density in the septa in L4 (Almási et al., 2019). We attempted to verify the
194 reported differential SST+ and VIP+ neuronal distributions using an alternative imaging
195 and counting strategy. To label the two neuronal populations, we crossed the SST-Cre
196 and VIP-Cre lines with a tdTomato reporter mouse line (Ai14). To comprehensively
197 quantify the density of SST+ and VIP+ cells in the barrel and septa domains in 3D, we
198 utilized a passive CLARITY-based tissue clearing protocol, followed by light-sheet
199 microscopy using a custom-built light-sheet microscope (Vladimirov et al., 2023; Voigt et
200 al., 2019) (Figure 2A). The individual barrels in wS1 were reliably detected using auto-
201 fluorescence from the tissue acquired with a 488nm laser. tdTomato positive SST+ or
202 VIP+ neurons were detected by a 561nm laser, allowing us to accurately localize and
203 count cells in barrel and septal domains (Figure 2B and C). By adjusting the angle of each
204 barrel column in 3D (using Imaris, RRID:SCR_007370), we precisely identified the
205 column through L2/3, L4 and L5, using the barrel borders for every plane (XY, YZ, XZ)
206 in L4 (Figure 2B, also see Methods). Once the columns were accurately determined, we
207 counted the number of tdTomato positive neurons in the barrels and septa and
208 corresponding volumes for density estimation. Despite their opposite distributions and
209 neuronal density changes along the depth of wS1 (Figure 2B and C), we found that both
210 SST+ (Figure 2D) and VIP+ (Figure 2E) neuronal densities were higher in L4 septa
211 compared to barrels, but we detected no difference in L2/3 and L5.
212 These results confirmed that SST+ and VIP+ interneurons have higher densities in septa
213 compared to barrels in L4 and suggest these interneurons may play a role in diverging
214 responses between barrels and septa upon SWS.
215
216 **SST+ neurons are more strongly activated by multi- versus single-whisker**
217 **stimulation**

218 Having identified spatial distribution patterns of SST+ or VIP+ interneurons that could
219 contribute to the single- vs multi- whisker response scaling observed in Figure 1F; we
220 sought to assess these interneurons' response profiles upon similar whisker stimulation
221 paradigms. Therefore, we performed similar SWS and MWS experiments using acute in-
222 vivo two-photon calcium (Ca2+) imaging under light anesthesia after weaning (P21–41)
223 (Figure 3A and B). We injected OGB-1, the membrane-permeable AM-ester form of the
224 calcium indicator, into wS1 of animals expressing tdTomato in either VIP+ or SST+ INs
225 (VIPCre-Ai14 and SSTCre-Ai14 lines, respectively) to localize VIP+ and SST+ activity
226 (Figure 3A). Two-photon Ca2+ imaging was performed upon stimulation of either the
227 principal C2 whisker at 10Hz for 2s (SWS) or most of the macro vibrissae including C2
228 (MWS) (Figure 3B). We found that both SST+ and VIP+ interneurons increased their firing
229 upon SWS (Figure 3C and D) as has been reported previously (Kastli et al., 2020), but
230 only SST+ interneurons changed their firing significantly between single- and multi-
231 whisker stimulation at 10-Hz (Figure 3D, SW vs MW comparison). Although these optical
232 recordings were performed in layer 2/3 (L2/3) rather than layer 4 (L4) due to depth
233 limitations, the similarity of the peak MW/SW ratios of L2/3 populations in putative barrel
234 and septa columns (c.f. Figure 1F and Supp. Figure 3) provides support for the validity of
235 using L2/3 data to infer respective L4 cell activity. This result suggests that differential
236 activation of SST+ interneurons is more likely to be involved in the domain specific
237 temporal ratio differences between barrels and septa.
238
239 **Progressive multi- over single-whisker response divergence in septal populations**
240 **is abolished in Elfn1 KO mice**
241 SST+ interneurons in the cortex are known to show distinct short-term synaptic plasticity,
242 particularly strong facilitation of excitatory inputs, which enables them to regulate the
243 temporal dynamics of cortical circuits. This facilitation allows SST+ cells to progressively
244 enhance their inhibitory influence in response to repeated stimulation, a property critical
245 for shaping network activity. A key regulator of this plasticity is the synaptic protein Elfn1,
246 which mediates short-term synaptic facilitation of excitation on SST+ interneurons
247 (Stachniak et al., 2021, 2019; Tomioka et al., 2014).

248 Having identified SST+ cells as potential regulators of temporal MW/SW ratio divergence,
249 we investigated how the absence of Elfn1 alters sensory-driven activity in vivo, potentially
250 shaping septal function in MW/SW response scaling. Using the same whisker stimulation
251 paradigms and domain-assignment strategy as in WT animals (Figure 1A and B; and
252 Supp. Figure 1), we recorded from barrel and septa domains in Elfn1 KO mice under both
253 single-whisker stimulation (SWS) and multi-whisker stimulation (MWS) conditions.
254 Unsupervised t-SNE analysis revealed that the domain-specific clustering of responses
255 seen in WT (Figure 1C) mice was disrupted in Elfn1 KO mice, with barrel and septa
256 responses intermingling (Figure 4A). This convergence of response profiles was further
257 clear in stimulus-aligned stacked images, where the emergent differences between
258 barrels and septa under SWS were largely abolished in the KO (Figure 4B). The only
259 remaining distinction was between directly stimulated barrels and neighboring barrels,
260 which persisted in the KO (Figure 4B). Under MWS conditions, the temporal divergence
261 between barrel and septa domains observed in WT Layer 4 was diminished in Elfn1 KO
262 mice (Figure 4C). Additionally, the progressive increase in the MW/SW response ratio
263 seen in septal neurons of WT mice was no longer seen in the KO (Figure 4D).
264 These findings suggest that in WT animals, activity spillover from principal barrels is
265 normally constrained by the progressive engagement of SST+ interneurons, driven by
266 Elfn1-dependent facilitation at their excitatory synapses. In the absence of Elfn1, this local
267 inhibitory mechanism is disrupted, leading to a loss of the distinct temporal response
268 divergence between barrel and septa domains.
269
270 **Barrel and Septa response decoding identity is lost in Elfn1 KO mice**
271 Building on our findings that Elfn1-dependent facilitation in SST+ interneurons is critical
272 for maintaining barrel-septa response divergence, we sought to quantify how sensory
273 information accumulates and is integrated over time in these domains—and how this
274 process is altered in Elfn1 KO mice.
275 To investigate this, we performed an accumulative temporal decoding analysis using
276 neural responses to 20 pulses of either single-whisker stimulation (SWS) or multi-whisker
277 stimulation (MWS) at 10 Hz for 2 seconds. We segmented the response window into three
278 time ranges to identify the temporal segments driving divergence between domains: the

full response window (1-95ms), the first part (1-50ms) which includes the first peak, and the late part (51-95ms), which includes the second firing peal (Figure 5A). A one-versus-all error-correcting output code (ECOC) classifier, using a GentleBoost ensemble of decision trees (Allwein et al., 2001; Friedman et al., 2000), was trained on firing profiles from WT barrel, septa, and neighboring barrel domains (3-class classification for SWS) or barrel and septa domains (2-class classification for MWS). We conducted 10-fold cross-validation within WT and KO datasets (WT CrossVal and KO CrossVal) and tested a WT-trained classifier on Elfn1 KO responses (WT Train - KO Test) to evaluate decoding performance across accumulated pulses (see Methods).

In WT mice, decoding accuracy increased progressively with the number of pulses upon SWS (Figure 5B, red) reflecting accumulated segregation of sensory information over time. This SWS WT CrossVal trend was more pronounced in the first response window (1-50ms) (Figure 5C vs 5D, red), indicating that domain-specific information accumulates predominantly in first temporal segments in repeated single whisker sampling. Cross-validation within the WT dataset (WT CrossVal) showed higher accuracy compared to the WT-trained classifier tested on KO responses (WT Train - KO Test) and KO CrossVal at this first segment, but not in the second (Figure 5B-D). Elfn1 KO dataset showed higher cross validation performance at the second part of the response profiles (Figure 5D) indicating a temporal information delay under the reduced progressive inhibition. While decoding curves started at similar initial levels for SWS data (Figures 5B-D, first pulse number), initial MW decoding accuracies were remarkably different (Figures 5E-G). In WT mice, while the decoding accuracy increased progressively as in SWS (Figure 5E, red), the difference between accumulated 20$^{th}$ and the starting (1$^{st}$) accuracies were lower than KO CrossVal results (Figures 5E-G, red vs blue) which was predominantly due to the first part of the signal (Figure 5F vs 5G).

These results highlight the critical role of Elfn1 in facilitating the temporal integration of sensory inputs through its effects on SST+ interneurons. In WT mice, Elfn1-dependent short-term facilitation enables SST+ interneurons to progressively enhance their inhibitory influence, maintaining the functional segregation between barrel and septa domains. In Elfn1 KO mice, the loss of this facilitation mechanism disrupts the temporal dynamics necessary for accumulating domain-specific information, leading to a failure in

310 segregating sensory streams. This finding reinforces the importance of local inhibitory
311 circuits, particularly those involving SST+ interneurons, in shaping the temporal
312 processing of sensory information in the barrel cortex.
313
314 **wS1 Barrel Columns and Septal Domains have different wS2 and M1 Layer-**
315 **dependent projection preferences**
316 We identified that temporal MW/SW response divergence in septal populations is
317 abolished in Elfn1 KO mice. Given that barrel and septal compartments differentially
318 process sensory input over time, this raises the question of how these distinct streams of
319 information are relayed to downstream regions and whether they contribute to separate
320 functional pathways. Following up from this observation, we finally aimed to explore if the
321 projection targets of these two wS1 domains are distinct, in a similar manner to what has
322 been revealed for visual cortex domain projections (Meier et al., 2021). Previously, it has
323 been shown that cortical pyramidal neurons in wS1 exhibit distinct long-range projection
324 patterns and sensory tuning properties depending on their projection target (S2 or M1).
325 S2-projecting pyramidal neurons tend to have narrower receptive fields, are more likely
326 to be tuned to the columnar whisker and carry more precise sensory information about
327 whisker deflections. In contrast, M1-projecting pyramidal neurons are more broadly tuned,
328 integrating information from multiple whiskers, which aligns with their role in sensorimotor
329 integration and behavior (Sato and Svoboda, 2010; Yamashita et al., 2013). This data
330 could be suggestive of distinct localization of the different projection neurons in the
331 different wS1 domains. By utilizing *in vivo* retrograde AAV injections in two of the main
332 target cortical regions of wS1, we aimed to characterize the projections from wS1 to wS2
333 and M1.
334 We injected a retrograde AAV virus expressing GFP in wS2 or M1 in separate adult mice
335 and dissected the brains 4 weeks after the injection (Figure 6A). We utilized again the
336 passive CLARITY-based tissue clearing and imaged the whole brain using mesoSPIM.
337 The auto-fluorescence of the barrels allowed for labeling of barrel columns in 3D (Figure
338 6B). With the same strategy as our previous analysis on interneuron population
339 distributions (Figure 2), we counted the number of neurons in wS1 barrel and septa
340 domains across the cortical layers (Figure 6C) and measured the corresponding domain

volumes to estimate projection densities as a proxy for connectivity levels between S1-S2 and S1-M1.

As an internal control and in line with expectations, fewer projections arose from layer 4 barrels to either wS2 or M1 than from other cortical layers (Figure 6C and D). However, septa cells between mid-L4 and upper-L5B sent more wS2 projections (Figure 6D, left, turquois), whereas more neurons in septa from L3 to L4 project to M1, compared to the projection cells in barrels (Figure 6D, right, magenta). Additionally, a secondary comparative analysis showed that barrels in L3 host significantly more wS2-projecting-neurons (Figure 6E, left, purple), while L5A septal domains host significantly more M1-projecting neurons (Figure 6E, right, magenta). This differential targeting suggests that the temporal whisker-evoked processing specialization of barrel and septa domains may shape how distinct streams of sensory information are conveyed to higher-order cortical areas, potentially influencing perceptual processing in wS2 and sensorimotor integration in M1.

## Discussion

In the absence of visual stimuli, humans explore objects through tactile interactions, where the initial touch begins the process of information accumulation, with subsequent touches refining the identification and characterization of the object. Rodents rely on a similar strategy during active whisking, where sequential whisker contacts allow for the progressive refinement of object recognition and spatial mapping (Armstrong-James and Fox, 1987; Kheradpezhouh et al., 2017; Petersen, 2007). This process involves parallel ascending pathways that transmit peripheral touch sensations to the cortex, with the primary somatosensory cortex mapping whisker spatial patterns directly onto cortical barrels, and in between spaces, septa (Van Der Loos and Woolsey, 1973; Woolsey et al., 1975).

Our study reveals that the functional segregation between barrel and septa domains in the mouse whisker primary somatosensory cortex (wS1) is not only anatomically defined by distinct thalamocortical projections but is also dynamically shaped by local inhibitory circuits, particularly those involving somatostatin-positive (SST+) interneurons. Through a combination of functional and anatomical techniques, we show that the temporal

372 divergence in spiking activity between barrel and septa domains is mediated by the short-
373 term synaptic facilitation properties of SST+ interneurons and are critically dependent on
374 the synaptic protein Elfn1. Furthermore, using a decoder we show that this temporal
375 divergence may affect the integration of sensory information during repeated whisker
376 stimulation, which may be subsequently routed to differential downstream cortical areas,
377 such as the secondary somatosensory cortex (wS2) and primary motor cortex (M1).
378 Among the inhibitory neuron classes, SST+ interneurons are known for their high
379 spontaneous activity and powerful regulation of local neural networks through dense
380 feedback connections onto nearby pyramidal neurons (Urban-Ciecko and Barth, 2016).
381 In contrast, VIP+ interneurons influence network function through a disinhibitory circuit,
382 inhibiting SST+ (and to a lesser extent PV+) interneurons upon activation, which in turn
383 reduces inhibition on pyramidal cells (Karnani et al., 2016; Lee et al., 2013; Pi et al., 2013).
384 Thus SST+ interneurons may contribute to barrel-septal identity using surround inhibition,
385 while being regulated themselves by VIP+ interneuron activity under certain behaviorally
386 relevant sensory-motor tasks. Our analysis of SST+ cell distribution, shows a higher
387 density in the septa in L4, compared to barrels. Interestingly, layer 4 SST+ interneuron
388 axons remain within layer 4 (Xu et al., 2013) in the somatosensory cortex, unlike SST+ of
389 layers 2/3 and 5/6 which are Martinotti type and target layer 1. In addition, while Martinotti
390 cells receive facilitating synapses from pyramidal cells and form inhibitory synapses onto
391 dendrites of neighboring pyramidal cells (Silberberg and Markram, 2007), non-Martinotti
392 SST cells predominantly inhibit fast spiking cells in layer 4 (Ma et al., 2006; Xu et al.,
393 2013). During naturalistic whisking, SST+ and PV+ cells show divergent activation
394 patterns, with FS cells showing transient excitation due to rapid synaptic depression,
395 while SST+ cells show the opposite (Tan et al., 2008). It is currently unclear though under
396 which behavioral circumstances SST+ cells of L4 would engage in inhibition of excitatory
397 cells versus inhibition of PV+ cells. Our data suggest that under our experimental
398 conditions, a bottom-up activation paradigm, SST+ cells overall engage in the progressive
399 inhibition of the local L4 circuit, rather than disinhibition. To assess whether temporal
400 divergence in spiking carries meaningful sensory information, we conducted a detailed
401 accumulative temporal decoding analysis. We find that in wild-type mice, decoding
402 accuracy for SWS increased progressively with each additional pulse, particularly in the

403 initial response window (1-50ms), indicating that domain-specific information
404 accumulates primarily in early temporal segments during repeated whisker sampling. This
405 progressive accumulation of decodable information was severely disrupted in Elfn1 KO
406 mice, with cross-validation showing significantly reduced performance compared to wild-
407 type, especially in early response segments. Interestingly, Elfn1 KO mice showed higher
408 cross-validation performance in the later response segment (51-95ms), suggesting a
409 temporal delay in information processing due to reduced progressive inhibition. Under
410 multi-whisker stimulation, wild-type and knockout mice showed markedly different initial
411 decoding accuracies, with the difference between accumulated and initial accuracies
412 being lower in wild-type than in Elfn1 KO mice. Our anatomical connectivity mapping
413 would suggest that disruption in temporal information processing in the two domains is
414 crucial for maintaining the functional segregation of parallel processing streams to wS2
415 and M1.
416 The differential projection patterns of barrel and septa domains to wS2 and M1 further
417 suggest that the temporal processing capabilities of these domains influence how sensory
418 information is integrated with motor output. For example, the projection of septa domains
419 to M1 may facilitate the rapid translation of sensory information into motor commands,
420 while the projection of barrel domains to wS2 may support more detailed sensory
421 discrimination. The disruption of the informational integrity of these projections in Elfn1
422 KO mice could therefore have significant implications for sensorimotor integration and
423 behavior.
424 It is important to note that while our study focuses on the mouse barrel cortex, there are
425 significant differences between rodent species, such as rats and mice, in terms of cortical
426 organization and whisker system function. Most research on whisker stimulation had
427 traditionally focused on rats (Estebanez et al., 2016; Petersen, 2007; Roy et al., 2011;
428 Tanke et al., 2018). The existence of septa in the mouse barrel cortex has been debated,
429 with some suggesting that the distinction between barrel and septal circuits is less
430 pronounced in mice compared to rats (Bureau et al., 2006; Sato et al., 2007). For
431 example, the mouse barrel cortex has fewer neurons per column and thinner septa
432 compared to rats, which may influence the degree of functional segregation between
433 barrel and septa domains. While many animals have whiskers, only a subset of animals

have visible cortical barrels. For instance, cats have whiskers and brainstem barrelettes but lack cortical barrels (Nomura et al., 1986; Rice, 1985; Rice et al., 1985). The presence of barrels in the cortex seems to correlate with volitional whisking behavior, underlining the importance of one-to-one mapping for processing individual whisker information. Our findings show that septa are crucial in separating these parallel whisker streams by modulating the lateral cortico-cortical information flow during repetitive whisker touches. This modulation is significantly influenced by the short-term facilitation properties of synaptic inputs onto SST+ interneurons, facilitated by the Elfn1 gene, alongside distinct bottom-up inputs to each domain. The loss of temporal segregation in Elfn1 KO mice could hinder object localization, which relies on multi-whisker integration in septa, while sparing simpler detection tasks mediated by barrels.

In summary, our study demonstrates that there exist a functional segregation of barrel and septa domains in the mouse whisker somatosensory cortex, and that is dynamically shaped by the temporal dynamics of SST+ interneuron activity, imparted by the synaptic protein Elfn1. This temporal divergence is essential for the integration of sensory information over repeated stimulation and for the differential projection of information to downstream cortical areas. These findings highlight the importance of local inhibitory circuits in shaping cortical processing and offer new insights into mechanisms underlying sensory perception and behavior.

**Acknowledgments**

We thank members of the Karayannis lab for suggestions and comments on the manuscript. Authors also thank George Kanatouris for helping with animal handling and breeding.

**Funding**

This work was supported by Swiss National Science Foundation Grant S-41260-01-01 (T.K) and European Research Council Grant 679175 (T.K).

**Author Contributions**

A.Ö.A. curated the data, analyzed in-vivo silicon probe recordings and the two-photon calcium imaging data, performed the decoder analysis and wrote the manuscript. T.J.S. conceptualized the study, maintained Elfn1 KO line, performed earlier electrophysiological characterizations and contributed to the drafting of the manuscript, J.W.Y. performed silicon probe recordings, AvdB collected two-photon calcium imaging data, L.C. performed light-sheet data analysis, R.K. performed tissue clearing and light-sheet image acquisition, T.K. conceptualized and supervised the study and wrote the manuscript.

**Declaration of Interest**

The authors declare no competing interests.

**Methods**

RESOURCE AVAILABILITY

Lead Contact

Further information and requests for resources and reagents should be directed to the Lead Contact, T.K. (karayannis@hifo.uzh.ch)

Materials Availability

This study did not generate new unique reagents.

Data and Code Availability

The datasets and analysis routines are available from the first author on reasonable request.

**Mice**

All the animal experiments followed the guidelines of the Veterinary Office of Switzerland and were approved by the Cantonal Veterinary Office Zurich and the University of Zurich. husbandry with a 12-h reverse dark-light cycle (7 a.m. to 7 p.m. dark) at 24 °C and variable humidity. Adult (5- to 10-week-old) male C57BL6J wide type mice were used for

495 retrograde tracing. Animal lines used in this study are VIP-IRES-Cre
496 (Vip$^{tm1(cre)Zjh}$/J)(Taniguchi et al., 2011), SST-IRES-Cre (Sst$^{tm2.1(cre)Zjh}$/J) (Taniguchi et al.,
497 2011), Ai14 (B6;129S6-Gt(ROSA)26Sor$^{tm14(CAG-tdTomato)Hze}$/J)(Madisen et al., 2010) and
498 Elfn1 KO (Elfn1tm1(KOMP)Vlcg). Both male and female mice were used in all
499 experiments.
500
501 **In-Vivo Silicon Probe Recording**
502 We used 4 Elfn1 KO and 4 WT littermates at the age of P20 to P30 for the multi-electrode
503 silicon probe recordings. Mice were under urethane induced anesthesia (1.5g/1kg)
504 throughout the experiment. A heating pad was used to maintain the mouse's body
505 temperature at 37°C. The depth of anesthesia was checked with breathing speed and
506 paw reflexes throughout the experiment. The skull of the right hemisphere was exposed
507 by removing the skin on top, and a metallic head holder was implanted on the skull with
508 cyanoacrylate glue and dental cement. A 26G needle was used to open a ~2mm x 2mm
509 cranial window which exposed the S1 barrel field (wS1). Extreme care was taken not to
510 cause damage or surface bleeding during surgery.
511 wS1 neural activities were recorded with an 8-shank-64-channel silicon probe. Each of
512 the 8 shanks has 8 recording sites (100μm apart). The distance between each shank is
513 200μm (NeuroNexus Technologies, Ann Arbor, MI, USA). The silicon probe was labeled
514 with DiI (1,1′-dioctadecyl-3,3,3′,3′-tetramethylindocarbocyanine, Molecular Probes,
515 Eugene, OR, USA) and inserted perpendicularly into the barrel cortex. A silver wire was
516 placed into the cerebellum as a ground electrode. All data were acquired at 20 kHz and
517 stored with MC Rack (RRID:SCR_014955) software (Multi Channel systems). The total
518 duration of multi-electrode recordings varied between 3 to 5 hours. After each experiment,
519 the animal was deeply anesthetized by ketamine (120 mg/kg, ketamine, 50 mg/mL,
520 HamelnPharma, Hameln Germany) and perfused through the aorta with ringer solution.
521 The brain was kept in 4% PFA. Tangential sections (200-μm thick) were prepared for
522 vesicular glutamate transporter 2 (vGlut2, Synaptic Systems, 135404; 1:1000)
523 immunohistochemistry. By combining the DiI and vGlut2 staining, the insertion position of
524 the 8 shank probes were identified in the barrel cortex.
525

526 **Whisker Stimulation**

527 Either a single principal whisker (SW, single whisker) or multiple whiskers (MW, multi
528 whisker) were stimulated 1mm from the snout in rostral-to caudal direction (about 1mm
529 displacement) using a stainless-steel rod (1 mm diameter) connected to a miniature
530 solenoid actuator. The movement of the tip of the stimulator bar was measured precisely
531 using a laser micrometer (MX series, Metralight, CA, USA) with a 2500 Hz sampling rate.
532 The stimulus takes 26ms to reach the maximal 1 mm whisker displacement, with a total
533 duration of 60ms until it reaches baseline (Yang et al., 2017). Both SW and MW
534 stimulation was performed at 10Hz for 2s and each stimulation repeated for 20 times (20
535 Trials). The inter-trial interval was 30s. In every experiment, multiple whiskers were singly
536 stimulated to increase the probability of finding a proximal barrel-septa and neighboring
537 barrel triplets. We first performed multi-whisker stimulation and then individual single
538 whisker stimulations were performed at the end. Individual whisker stimulation was
539 performed by attaching a pipet tip to the stimulator, which was then placed in contact with
540 the principal whisker under a dissecting scope. MW stimulation was performed by
541 contacting multiple whiskers with 1cm-wide masking tape attached to the pipet tip.

542

543 **In vivo two-photon calcium imaging**

544 Neuronal ensembles in superficial layers of the principal whisker barrel field mapped by
545 intrinsic signal imaging were bolus-loaded with the AM ester form of Oregon Green
546 BAPTA-1 by pressure injection (OGB-1; 1 mM solution in $Ca^{2+}$-free Ringer's solution; 2-
547 min injection at 150–200 μm depth) as described previously (Stosiek et al., 2003). The
548 craniotomy was then filled with agarose (type III-A, 1% in Ringer's solution; Sigma) and
549 covered with an immobilized glass plate. Two-photon $Ca^{2+}$ imaging was performed with
550 a Scientifica HyperScope two-photon laser scanning microscope one hour after bolus
551 loading using a Ti:sapphire laser system at 900 nm excitation (Coherent Chameleon;
552 ~120 femtosecond laser pulses). Two-channel fluorescence images of 256 × 128 pixels
553 at 11.25 Hz (HyperScope galvo-mode) were collected with a 16x water-immersion
554 objective lens (Nikon, NA 0.8). In all, 3–5 separate spots have been imaged per animal.
555 Per imaging spot, 10 trials of 20s-long evoked activity recorded for each of single- and

556 multi- whisker stimulation paradigms. Data acquisition was controlled by ScanImage
557 (Pologruto et al., 2003).
558
559 **Analysis of calcium imaging data**
560 $Ca^{2+}$ imaging data is analyzed using custom MATLAB scripts. First, fluorescence image
561 time-series for a given region were concatenated. The concatenated data was then
562 aligned using a Fourier domain cross-correlation based subpixel registration algorithm
563 (Guizar-Sicairos et al., 2008) to correct for translational drift (registered on red tdTomato
564 channel and transferred to OGB-1 channel). Average intensity projections of the imaging
565 data were used as reference images to manually annotate regions of interest (ROIs)
566 corresponding to individual neurons. Neurons with somata partly out-of-focus were not
567 included. $Ca^{2+}$ signals were expressed as the mean pixel value of the relative
568 fluorescence change $\Delta F/F = (F-F_0)/F_0$ in each given ROI. $F_0$ was calculated as the bottom
569 5% of the fluorescence trace. Neuropil patches surrounding each neuron is defined by all
570 pixels not assigned to a neuronal soma or astrocyte of the corresponding neuron ROI
571 annotation (Peron et al., 2015) (A disk shaped region around the neuron of interest with
572 excluding any intersecting neighboring neuronal ROI). Neuropil correction is performed
573 as $F_{corrected} = F_{neuron} - \alpha * F_{neuropil}$. α is estimated for each imaging spot separately using the
574 formula $F_{blood_vessel}/F_{surrounding_neuropil}$ (Kerlin et al., 2010). For each stimulus, the evoked
575 responses of 10 trials were analyzed and the response magnitude expressed as the mean
576 of the evoked $\Delta F/F$ integral (%·s; integral of the first 2s response starting at stimulus
577 onset).
578
579 **Analysis of Silicon Probe Data**
580 Extracellular silicon probe data were analyzed using a custom-made Matlab script
581 (MATLAB (RRID:SCR_001622), Version: 2024a, MathWorks, MA, USA). The raw data
582 signal was band-pass filtered (0.8-5 kHz), and the multi-unit activity (MUA) was extracted
583 with the threshold of 7.5 times the standard deviation (SD) of baseline (Yang et al., 2017).
584 The current source density (CSD) map was used to identify laminar probe contact
585 location. The earliest CSD sink was identified as layer 4, followed by L2-3 (Reyes-Puerta

et al., 2015; Van Der Bourg et al., 2017). MUA was smoothed using a Gaussian kernel (0 mean, 5ms sigma).

**Decoder Analysis**

Recordings from the principal barrel, adjacent septa, and a neighboring unstimulated barrel were organized into three matrices for wild-type (WT) animals: a 280 × 95 × 20 matrix for the stimulated barrel (14 Barrels, 95ms, 20 pulses), a 180 × 95 × 20 matrix for the septa (9 Septa, 95ms, 20 pulses), and a 360 × 95 × 20 matrix for the neighboring barrel (18 Neighboring barrels, 95ms, 20 pulses). Each matrix's dimensions correspond to the number of recording channels, time points (95ms epochs), and 20 individual stimulation trials, respectively. Although each trial originally spanned 2000ms (20 pulses at 10Hz), the analysis focused on the first 95ms post-stimulation (95ms instead of 100ms). To examine the impact of different temporal windows on classification performance, three versions of the analysis were performed by varying the time-range parameter, 1 to 95ms for the full epoch, 1 to 50ms for the first part, and 51 to 95ms for the second part.

For each stimulation trial, data was accumulated pulse-by-pulse. In each iteration (ranging from 1 to 20), the corresponding segments from the three matrices were reshaped into two-dimensional feature matrices by concatenating the selected time points across the accumulated pulses. Labels were then assigned to the reshaped data ('B' for the barrel, 'S' for septa, and 'N' for the neighboring barrel).

We employed a classification approach utilizing error-correcting output codes (ECOC) models with a gentle adaptive boosting (GentleBoost) strategy to train classifiers. This method is particularly effective in handling imbalanced data and unequal misclassification costs. Like Logit Boost, each weak learner in the ensemble fitted a regression model to response values, $y_n \in \{-1, +1\}$. The mean-squared error is computed as:

$$N \sum_{n=0}^{d} d(t)_n \left(y_n - h_t(x_n)\right)^2$$

where $d(t)_n$ represents observation weights at step t (summing up to 1) and $h_t(x_n)$ denotes predictions from the regression model $h_t$ fitted to response values $y_n$. As the

strength of individual learners diminishes, the weighted mean-squared error converges towards 1.

Three distinct evaluations were performed. WT-to-KO Prediction, the ECOC classifier trained on WT data (compiled from the three regions) was used to predict labels from corresponding recordings in knockout (KO) mice. Within-Group Cross-Validation (WT), A cross-validation procedure was applied to the WT dataset using MATLAB's *crossval* function to assess classifier performance internally. Within-Group Cross-Validation (KO), Similarly, an ECOC classifier was trained and cross-validated on the KO dataset.

For each evaluation, confusion matrices were generated and summary accuracy statistics computed. Accuracy was tracked as a function of the number of accumulated pulses (from 1 to 20). The accuracy value represents the average per-class accuracy. In other words, for each class the accuracy is defined as: $\text{Accuracy}_{\text{class}}$ = (TP + TN) / Total samples, where for that class, TP (True Positives) is the number of correctly predicted samples (the corresponding diagonal element of the confusion matrix), and TN (True Negatives) is the sum of all correct predictions for samples not in that class (i.e., all the entries outside the row and column of that class). The function first computes the confusion matrix C where rows represent actual classes and columns represent predicted classes. It then calculates the total number of samples as the sum of all entries in C, and it determines the number of classes. The overall accuracy reported is computed via the formula:

Accuracy = (2*trace(C)+2*Total)/((Number of Classes)*Total)

Here, trace(C) is the sum of the diagonal elements, which means it is the sum of the true positives for all classes, and *Total* is the sum of all entries in the confusion matrix. Although this formula may look a bit unusual, it is designed to yield the average of the per-class accuracies. In practice, for each class, one would compute (TP + TN) / Total and then average these values over the classes that reflects how well the classifier performed across all classes. To characterize the evolution of classification accuracy with increasing pulse number, non-linear exponential functions of the form:

$$f(x) = a - b * \exp(-cx)$$

were fitted to the accuracy data using a non-linear least squares approach (implemented via the *fminspleas* function). Separate fits were obtained for the WT-to-KO prediction, WT

646 cross-validation, and KO cross-validation accuracy curves. The fitted curves and raw
647 accuracy data were then plotted. This integrated analysis pipeline allowed for systematic
648 comparison of classification performance across spatial locations and conditions and an
649 assessment of the temporal dynamics underlying the neural responses to single-whisker
650 stimulation. The same strategy has been used for multi-whisker decoding but between
651 only Barrel and Septa.
652
653 **Retrograde tracing**
654 Mice aged from P10-37 were anesthetized by isoflurane and a small craniotomy was
655 made above the injection site (M1 or S2). 200nl retrograde AAV virus, ssAAV-retro/2-
656 CAG-EGFP-WPRE-SV40p(A) (physical titer: $5X10^{12}$ vg/ml) was injected 200-500μm
657 deep in the M1 or S2. Virus was purchased from Zurich Viral Vector Facility (Cat#: V24-
658 retro).
659
660 **Tissue Processing for Passive Clearing and Imaging**
661 The method used for hydrogel-based tissue clearing is explained in detail elsewhere
662 (Chung and Deisseroth, 2013). Briefly, Mice age P29-70 (4 weeks after retrograde AAV
663 virus injection) or SST-Ai14 and VIP-Ai14 mice age from P14-77 were transcardially
664 perfused using 1x PBS and Hydrogel solution (1% PFA, 4% Acrylamide, 0.05% Bis). The
665 collected brains were post-fixed for 48 h in a Hydrogel solution (1% PFA, 4% Acrylamide,
666 0.05% Bis). Afterward, the Hydrogel polymerization was induced at 37 °C. Following the
667 polymerization, the brains were immersed in 40 mL of 8% SDS and kept shaking at room
668 temperature until the tissue was cleared sufficiently (15-90 days depending on the
669 animal's age). Finally, after 2–4 washes in PBS, the brains were put into a self-made
670 refractive index matching solution (RIMS). They were left to equilibrate in 5 mL of RIMS
671 for at least 4 days at RT (Room Temperature) before being imaged. After clearing, brains
672 were attached to a small weight and loaded into a quartz cuvette, then submerged in
673 RIMS, and imaged using a home-built mesoscale selective plane illumination microscope
674 (mesoSPIM, Voigt et al., 2019). The microscope consists of a dual-sided excitation path
675 using a fiber-coupled multiline laser combiner (405, 488, 515, 561, 594, 647 nm, Omicron
676 SOLE-6) and a detection path comprising an Olympus MVX-10 zoom macroscope with a

677 1× objective (Olympus MVPLAPO 1x), a filter wheel (Ludl 96A350), and a scientific CMOS
678 (sCMOS) camera (Hamamatsu Orca Flash 4.0 V3). For imaging tdTomato and eGFP a
679 594 nm excitation with a 594 long-pass filter (594 LP Edge Basic, AHF) and 488 nm &
680 520/35 (BrightLine HC, AHF) were used, respectively. The excitation paths also contain
681 galvo scanners (GCM-2280-1500, Citizen Chiba) for light-sheet generation and reduction
682 of streaking artifacts due to absorption of the light-sheet. In addition, the beam waist is
683 scanning using electrically tunable lenses (ETL, Optotune EL-16-40-5D-TC-L)
684 synchronized with the rolling shutter of the sCMOS camera. This axially scanned light-
685 sheet mode (ASLM) leads to a uniform axial resolution across the field-of-view of 5–10 μm
686 (depending on zoom and wavelength). The magnification 0.8X (pixel size: 8.23 μm) was
687 used for the view of the whole brain and 2X (pixel size: 3.26 μm) was used for the view
688 of barrel cortex. Further technical details of the mesoSPIM are described elsewhere
689 (Vladimirov et al., 2023; Voigt et al., 2019).
690

691 **Analysis of cleared brain imaging data**

692 Barrel cortex was imaged in 3D with 2X objective. The images were processed through
693 Fiji and Imaris to visualize the 3D structure of the barrel cortex. XY-, YZ-, XZ- projections
694 were visualized in Imaris, which allows us to adjust the correct angle for each barrel
695 column to be vertical against XY-plane. This method allowed us identify barrel and septa
696 in layers 2-3 and 5 and layer 4. In addition, the depth information is also precisely acquired
697 for each barrel column. SST+ or VIP+ neuron numbers, S2-projected and M1-projected
698 S1 neuron numbers were counted in icy. Max projection for each 50 ums along barrel
699 columns was acquired and neurons on each max projection image were counted
700 automatically by icy (RRID:SCR_010587) with the same threshold for all the brains. Each
701 barrel was drawn according to the barrel map from each brain by max projection. The
702 area of septa was calculated by subtracting the whole selected area from all the selected
703 barrel areas.
704

705 **t-SNE Analysis**

706 To visualize the segregation of neural responses across the different cortical domains,
707 we applied t-distributed Stochastic Neighbor Embedding (t-SNE) to the averaged

datasets. t-SNE was used to reduce the high-dimensional data into a 2D space for visualization. The parameters for t-SNE were set to use the *barneshut* algorithm for efficiency, with a perplexity of 9 and exaggeration of 3 to enhance cluster separation. The resulting t-SNE coordinates were plotted using MATLAB's *gscatter* function to distinguish between the different domains (Barrel, Septa, Neighboring). This analysis allowed us to visually inspect the clustering of neural responses from different cortical domains.

**Statistical Analysis of the Multi-Unit Activity**

To evaluate the statistical significance of differences in multi-unit activity (MUA) responses between barrel (B), septa (S), and neighboring barrel (N) domains across 20 pulses of whisker stimulation, we performed a pulse-by-pulse comparison using the non-parametric Mann-Whitney U test (also known as the Wilcoxon rank-sum test). This analysis was conducted on the averaged MUA data recorded from Layer 4 of the whisker somatosensory cortex (wS1) in wild-type (WT) and Elfn1 knockout (KO) mice during single-whisker stimulation (SWS) and multi-whisker stimulation (MWS) paradigms, as detailed above. For each of the 20 stimulation pulses (1 to 20), the MUA data for each domain were reshaped and averaged across trials. The Mann-Whitney U test was then applied pairwise to assess differences between domains: barrel vs. septa (B vs S), barrel vs. neighboring barrel (B vs N), and septa vs. neighboring barrel (S vs N). The resulting p-values were stored in a 3×20 matrix, where rows correspond to the pairwise comparisons and columns represent the pulse number. To visualize the statistical outcomes, a heatmap was generated using MATLAB (Version 2024a, MathWorks, MA, USA). A custom discrete colormap was created by adapting the hot colormap, which originally provides a gradient of 10 colors ranging from black (low values) to white (high values). We selected specific indices from this gradient (10, 8, 6, 4, 2, 1) to define a 10-level discrete colormap, assigning the darkest shade (black) to p-values ≤ 0.05 (indicating statistical significance) and progressively lighter shades to higher p-values, with the lightest shade (white) representing p-values > 0.05. The colormap was inverted to ensure that significant p-values (≤ 0.05) appeared as light shades against a dark background, enhancing visual contrast. The heatmap was plotted with p-values scaled between 0 and 0.05, using the custom colormap.

739 **Statistical Analysis**

740 Data are represented as mean ± SEM unless stated otherwise. Statistical comparisons
741 have been done using a one-tailed Mann-Whitney-U test for non-paired data and one-
742 tailed Wilcoxon signed-rank test for paired comparisons (the statistical significance
743 threshold was set to $p<0.05$; in the Figures, different degrees of evidence against the null
744 hypothesis are indicated by asterisks ($p<0.05$: *; $p<0.01$: **; $p<0.001$: ***). Cell densities
745 in Figures 2 and 6 were compared using repeated measures ANOVA. All tests were
746 conducted using custom codes in Matlab.

747

748 **Figure Legends**

749 **Figure 1.** Temporal divergences emerge between barrel and septa domains upon
750 repeated whisker stimulation in Layer 4 of mouse wS1. (A) Either principal whiskers
751 (SWS, or single whisker) or most of the principal whiskers (MWS, or multi whisker) were
752 stimulated for 2s at 10Hz (20 pulses) for 20 times (20 trials). (B) Acute simultaneous *in-*
753 *vivo* silicon probe (8x8) recordings were performed from barrel and septa domains after
754 the start of active whisking (>P21) (C) t-SNE analysis of the average firing dynamics from
755 three domains after averaging 20 single trials. (D) Left: Average multi-unit firing profiles
756 recorded at Layer 4 of barrel (black), unstimulated neighbor (blue) and septa (pink)
757 columns upon 2s-long 10Hz repeated single whisker stimulation. Middle: Matrix
758 representation of the data. Right: Pair-wise statistical comparisons of first 50ms of the
759 responses (yellow line represents the cut off) of three conditions for all pulses (Mann-
760 Whitney-U-Test). (E) Same with E but response profiles upon MW stimulation. (F) Top:
761 Temporal ratio dynamics (average AUC MW responses divided by average AUC SW
762 responses) for barrel and septa. Bottom: statistical comparison of average AUC ratios of
763 all pulses (1-20), first six (1-6) or last 14 pulses (7-20), respectively. (p values are color
764 coded in D, stars represents *: $p<0.05$; **: $p<0.01$; ***: $p<0.001$ in E and F.)

765

766 **Figure 2.** SST+ and VIP+ neuron densities differ at Barrel and Septa Domains in Layer
767 4. (A) A passive CLARITY-based tissue clearing protocol was performed on the collected
768 brains which were subsequently imaged in their entirety using a custom-built light-sheet
769 microscope (mesoSPIM). 561nm wavelength was used to image tdTomato, 488nm

770 wavelength was used to image autofluorescence. (B) 3D reconstruction of cleared SST-
771 Ai14 (left) and VIP-Ai14 (right) barrel cortex. X-Y, X-Z and Y-Z views are presented
772 focusing with a single barrel max projection. The brain was rotated to achieve the
773 orientation that the barrel columns are perpendicular to the X-Y view. The scale bars are
774 set for 500µm. (C) Max projection examples of SST (red) and VIP (blue) neurons in wS1
775 L2-3, L4 and L5. Quantified barrels (yellow lines) and septa (green lines) are circled out
776 which are perpendicular to X-Y (top-down) view. The scale bar is set for 200µm. (D) SST+
777 neuron density distribution over laminae for barrel and septal domains (N=4 mice, n=54
778 Barrels and surrounding septa per barrel). Normalized cell densities plotted as a function
779 of depth. 0µm represents the top of layer 4. SST+ interneuron density is significantly
780 higher in septa (p=0.0015, F=30.64, repeated-measures ANOVA). (E) VIP+ neuron
781 density distribution over laminae for barrel and septal domains. (N=4 mice, n=53 Barrels
782 and surrounding septa per barrel). Normalized cell densities plotted as a function of depth.
783 0µm represents the top of layer 4. VIP+ interneuron density is also significantly higher in
784 septa (p=0.021, F=9.63, repeated-measures ANOVA).
785
786 **Figure 3**. Single- vs multi- whisker responses of SST+ and VIP+ Interneurons (A)
787 Interneurons are labeled with tdTomato using reporter mouse lines and $Ca^{2+}$ imaging has
788 been performed after bulk loading of OGB-1. scale bar 35µm. (B) Schematic
789 representation of the single- and multi- whisker stimulation protocol upon 10Hz
790 stimulation. (C) Δ*F/F* traces of evoked activity of SST (on top) and VIP (on bottom)
791 interneurons (*N* = 3 animals per group, VIP P21+: 138 cells, SST P21+: 51 cells). (D) Area
792 under the curve (AUC) of the first 2s of the Δ*F/F* traces of all SST and VIP cells upon
793 single- (SW: 2s-long principal whisker evoked activity) and multi- whisker (MW: 2s-long
794 multi whisker stimulation evoked activity) stimulation (Wilcoxon signed-rank test, Base:
795 2s-long baseline activity).
796
797 **Figure 4.** Loss of Elfn1 abolishes barrel-septa response divergences upon single-whisker
798 stimulation. (A) t-SNE analysis of the average firing dynamics from three domains. (B)
799 Left: Average multi-unit firing profiles recorded at Layer 4 of barrel (gray), unstimulated
800 neighbor (light blue) and septa (purple) columns (11-barrel columns, 7 septal columns,

801 11 unstimulated neighbors from N=4 mice) upon 2s-long 10Hz repeated single whisker
802 stimulation. Middle: Matrix representation of the same data by representing each
803 stimulation pulse response on one row. Bottom: Pair-wise statistical comparisons of three
804 conditions for all pulses (Mann-Whitney-U-Test). (C) Same with but response profiles
805 upon MW stimulation. (D) Top: Ratio of MW/SW dynamics for barrel and septa. Bottom:
806 statistical comparison of average ratios of 20 average of all pulses, first six or last 14
807 pulses, respectively. (p values are color coded in B, stars represents *: $p<0.05$; **: $p<0.01$;
808 ***: $p<0.001$ in C and D.)
809
810 **Figure 5.** Accumulative decoding analysis shows an alteration of columnar domain
811 identity in Elfn1 KO animals. (A) For the decoding analysis, the entire pulse response,
812 only the first 50ms or only the last 45ms has been used. (B) Decoder analysis of the full
813 pulse response profiles in L4 upon SWS. (C) Decoder analysis of the first part of the pulse
814 response (1-50ms) profiles in L4 upon SWS. (D) Decoder analysis of the second part of
815 the pulse response (51-95ms) profiles in L4 upon SWS. (E) Decoder analysis of the full
816 pulse response profiles in L4 upon MWS. (F) Decoder analysis of the first part of the pulse
817 response (1-50ms) profiles in L4 upon MWS (G) Decoder analysis of the second part of
818 the pulse response (51-95ms) profiles in L4 upon MWS.
819
820 **Figure 6.** wS1 barrel and septa columns differentially project to wS2 and M1 (A) The
821 schematics of the experimental protocol. The retro-AAV-CAG-GFP was injected in either
822 S2, or M1 at P20-30 and the brains were dissected 4 weeks after the virus injection
823 following the tissue clearing and whole brain imaging. (B) 3D reconstruction of the cleared
824 brain with S2(Left panels) or M1(right panels) injection. X-Y, X-Z and Y-Z views are
825 presented focus with a single barrel max projection. The brain was rotated to achieve the
826 orientation that the septa is perpendicular to the X-Y view (top-down). Scale bars in whole
827 brain view are set for 2000um and the scale bars in X-Y, X-Z and Y-Z views are set for
828 200um. (C) Max projection examples of S2-projected wS1 neurons and M1-projected
829 wS1 neurons in L2-3, L4 and L5 in barrel vs septa. Quantified barrels (yellow lines) and
830 septa (blue lines) are circled out which are perpendicular to X-Y (top-down) view. Scale
831 bars are set for 200um. (D) Left: Normalized cell density profiles of S2 projection neurons

832 at barrel and septa columns. 0μm represents the top of layer 4. L4 and L5a septa columns
833 send significantly more projections to S2 than barrel column (N=4 mice) (p=0.0139,
834 F=11.79, repeated-measures ANOVA). Right: Normalized cell density profiles of M1
835 projections neurons at barrel and septa columns. 0μm represents the top of layer 4. L3
836 and L4 septa columns send significantly more projections to M1 (N=6 mice) (p=0.0032,
837 F=14.82, repeated measures ANOVA). (E) Left: Normalized cell density profiles of S2
838 and M1 projection neurons at barrel columns. 0μm represents the top of L4. L3 barrel
839 columns send significantly more projections to S2 (N=4 mice with S2 injections, N=6 mice
840 with M1 injections) (p=0.0293, F=7.02, repeated-measures ANOVA). Right: Normalized
841 cell density profiles of S2 and M1 projections neurons at septa columns. 0μm represents
842 the top of L4. L5a septal columns send significantly more projections to M1 N=4 mice with
843 S2 injections, N=6 mice with M1 injections) (p=0.0402, F=5.98, repeated measures
844 ANOVA).
845
846 **Supplementary Figure 1.** An example of assignment of barrel, septa and Neighbor
847 electrodes using histology and current source density (CSD) analysis. (A) Shank
848 electrode map of 8x8 silicon probes. (B) Probe locations were labeled (DiI) after each
849 experiment using histology (vGlut2 staining). Matching shank locations are indicated
850 using yellow numbers. Blue dots represent the insertion sites. The red and white text
851 depicts corresponding barrel names (C) All principal whiskers are stimulated one-by-one.
852 C1 to C5 barrel responses upon single whisker stimulation are shown from top to bottom.
853 (D) A closer look on C1, C2 and C3 whisker stimulations and corresponding CSD at
854 shanks 5,6,7 and 8. (E), Barrel (B), adjacent septa (S) and the adjacent neighboring barrel
855 (N) were assigned according to the probe insertion sites and L4 barrel autofluorescence
856 in combination with CSD responses. For example, while shanks 6 and 8 show strong
857 response upon single whisker stimulation (and hence assigned as barrels), shank 7 does
858 not show the expected response (hence assigned as septa). Only the triplets of
859 electrodes were used in the analysis in which principal barrel (B), adjacent septa (S) and
860 the adjacent neighboring barrel (N) were captured by the probe insertion sites for any
861 experiment (Left). 14-barrel columns, 9 septal columns, 18 unstimulated neighboring
862 barrels from N=4 mice. (F) An ideal schematic representation (on the left). Realistically,

we cannot always be sure if an entire shank is consistently going through a barrel or septal column due to the curvature of the cortex (on the right) for above and below of layer4.

**Supplementary Figure 2.** Representation of the conversion of the two-second-long single trial recordings into 20x100ms matrices. (A) Schematic representation. (B) An example data. The last 5ms of each pulse have been discarded in further analysis.

**Supplementary Figure 3.** (A) Left: Average multi-unit firing profiles recorded at Layer 2/3 of barrel (black), unstimulated neighbor (blue) and septa (pink) columns upon 2s-long 10Hz repeated single whisker stimulation. Right: Another representation of the same data but converted into an image by representing each stimulation pulse response on one row. (B) Left: Average multi-unit firing profiles recorded at Layer 2/3 of barrel (black), unstimulated neighbor (blue) and septa (pink) columns upon 2s-long 10Hz repeated multi whisker stimulation. Right: Another representation of the same data but converted into an image by representing each stimulation pulse response on one row. (C) Left: Temporal ratio dynamics (average AUC MW responses divided by average AUC SW responses) for barrel and septa for layer2/3. Right: statistical comparison of average AUC ratios of all pulses (1-20), first six (1-6) or last 14 pulses (7-20), respectively (stars represents *: $p<0.05$; **: $p<0.01$; ***: $p<0.001$ in F and G. Wilcoxon rank sum test).

## References


Ahissar E, Sosnik R, Bagdasarian K, Haidarliu S. 2001. Temporal frequency of whisker movement. II. Laminar organization of cortical representations. *J Neurophysiol* **86**. doi:10.1152/jn.2001.86.1.354

Alloway KD. 2008. Information processing streams in rodent barrel cortex: The differential functions of barrel and septal circuits. *Cerebral Cortex*. doi:10.1093/cercor/bhm138

Allwein EL, Schapire RE, Singer Y. 2001. Reducing multiclass to binary: A unifying approach for margin classifiers. *Journal of Machine Learning Research* **1**.

Almási Z, Dávid C, Witte M, Staiger JF. 2019. Distribution patterns of three molecularly defined classes of gabaergic neurons across columnar compartments in mouse barrel cortex. *Front Neuroanat* **13**. doi:10.3389/fnana.2019.00045

Armstrong-James M, Fox K. 1987. Spatiotemporal convergence and divergence in the rat S1 “Barrel” cortex. *Journal of Comparative Neurology* **263**. doi:10.1002/cne.902630209

Audette NJ, Urban-Ciecko J, Matsushita M, Barth AL. 2018. POm Thalamocortical Input Drives Layer-Specific Microcircuits in Somatosensory Cortex. *Cereb Cortex* **28**. doi:10.1093/cercor/bhx044

Brecht M, Sakmann B. 2002. Dynamic representation of whisker deflection by synaptic potentials in spiny stellate and pyramidal cells in the barrels and septa of layer 4 rat somatosensory cortex. *Journal of Physiology*. doi:10.1113/jphysiol.2002.018465

Bureau I, Von Paul F Saint, Svoboda K. 2006. Interdigitated paralemniscal and lemniscal pathways in the mouse barrel cortex. *PLoS Biol* **4**. doi:10.1371/journal.pbio.0040382

Cai L, Yang JW, Wang CF, Chou SJ, Luhmann HJ, Karayannis T. 2022. Identification of a Developmental Switch in Information Transfer between Whisker S1 and S2 Cortex in Mice. *Journal of Neuroscience* **42**. doi:10.1523/JNEUROSCI.2246-21.2022

Carvell GE, Simons DJ. 1990. Biometric analyses of vibrissal tactile discrimination in the rat. *Journal of Neuroscience* **10**. doi:10.1523/jneurosci.10-08-02638.1990

Chakrabarti S, Alloway KD. 2006. Differential origin of projections from SI barrel cortex to the whisker representations in SII and MI. *Journal of Comparative Neurology* **498**. doi:10.1002/cne.21052

Chmielowska J, Carvell GE, Simons DJ. 1989. Spatial organization of thalamocortical and corticothalamic projection systems in the rat SmI barrel cortex. *Journal of Comparative Neurology* **285**. doi:10.1002/cne.902850304

Chung K, Deisseroth K. 2013. CLARITY for mapping the nervous system. *Nat Methods* **10**. doi:10.1038/nmeth.2481

Douglas RJ, Martin KAC. 2004. Neuronal circuits of the neocortex. *Annu Rev Neurosci*. doi:10.1146/annurev.neuro.27.070203.144152

Estebanez L, Bertherat J, Shulz DE, Bourdieu L, Léger JF. 2016. A radial map of multi-whisker correlation selectivity in the rat barrel cortex. *Nat Commun* **7**. doi:10.1038/ncomms13528

Friedman J, Hastie T, Tibshirani R. 2000. Additive logistic regression: A statistical view of boosting. *Ann Stat*. doi:10.1214/aos/1016218223

Grant RA, Mitchinson B, Prescott TJ. 2012. The development of whisker control in rats in relation to locomotion. *Dev Psychobiol* **54**. doi:10.1002/dev.20591

Guizar-Sicairos M, Thurman ST, Fienup JR. 2008. Efficient subpixel image registration algorithms. *Opt Lett* **33**. doi:10.1364/ol.33.000156

Karnani MMM, Jackson J, Ayzenshtat I, Tucciarone J, Manoocheri K, Snider WGG, Yuste R. 2016. Cooperative Subnetworks of Molecularly Similar Interneurons in Mouse Neocortex. *Neuron* **90**. doi:10.1016/j.neuron.2016.02.037

Kastli R, Vighagen R, van der Bourg A, Argunsah AÖ, Iqbal A, Voigt FF, Kirschenbaum D, Aguzzi A, Helmchen F, Karayannis T. 2020. Developmental divergence of sensory stimulus representation in cortical interneurons. *Nat Commun* **11**. doi:10.1038/s41467-020-19427-z

Kerlin AM, Andermann ML, Berezovskii VK, Reid RC. 2010. Broadly Tuned Response Properties of Diverse Inhibitory Neuron Subtypes in Mouse Visual Cortex. *Neuron* **67**. doi:10.1016/j.neuron.2010.08.002

Kheradpezhouh E, Adibi M, Arabzadeh E. 2017. Response dynamics of rat barrel cortex neurons to repeated sensory stimulation. *Sci Rep* **7**. doi:10.1038/s41598-017-11477-6

Kim U, Ebner FF. 1999. Barrels and septa: Separate circuits in rat barrel field cortex. *Journal of Comparative Neurology* **408**. doi:10.1002/(SICI)1096-9861(19990614)408:4<489::AID-CNE4>3.0.CO;2-E

Koralek KA, Jensen KF, Killackey HP. 1988. Evidence for two complementary patterns of thalamic input to the rat somatosensory cortex. *Brain Res* **463**. doi:10.1016/0006-8993(88)90408-8

Lee S, Kruglikov I, Huang ZJ, Fishell G, Rudy B. 2013. A disinhibitory circuit mediates motor integration in the somatosensory cortex. *Nat Neurosci* **16**. doi:10.1038/nn.3544

Ma Y, Hu H, Berrebi AS, Mathers PH, Agmon A. 2006. Distinct subtypes of somatostatin-containing neocortical interneurons revealed in transgenic mice. *Journal of Neuroscience* **26**. doi:10.1523/JNEUROSCI.0661-06.2006

Madisen L, Zwingman TA, Sunkin SM, Oh SW, Zariwala HA, Gu H, Ng LL, Palmiter RD, Hawrylycz MJ, Jones AR, Lein ES, Zeng H. 2010. A robust and high-throughput Cre reporting and characterization system for the whole mouse brain. *Nat Neurosci* **13**:133–140. doi:10.1038/nn.2467

Meier AM, Wang Q, Ji W, Ganachaud J, Burkhalter A. 2021. Modular network between postrhinal visual cortex, amygdala, and entorhinal cortex. *Journal of Neuroscience* **41**. doi:10.1523/JNEUROSCI.2185-20.2021

Melzer P, Champney GC, Maguire MJ, Ebner FF. 2006a. Rate code and temporal code for frequency of whisker stimulation in rat primary and secondary somatic sensory cortex. *Exp Brain Res* **172**:370–386. doi:10.1007/s00221-005-0334-1

Melzer P, Sachdev RNS, Jenkinson N, Ebner FF. 2006b. Stimulus frequency processing in awake rat barrel cortex. *Journal of Neuroscience* **26**. doi:10.1523/JNEUROSCI.2620-06.2006

Nomura S, Itoh K, Sugimoto T, Yasui Y, Kamiya H, Mizuno N. 1986. Mystacial vibrissae representation within the trigeminal sensory nuclei of the cat. *Journal of Comparative Neurology* **253**. doi:10.1002/cne.902530110

O'Connor DH, Hires SA, Guo Z V., Li N, Yu J, Sun QQ, Huber D, Svoboda K. 2013. Neural coding during active somatosensation revealed using illusory touch. *Nat Neurosci* **16**. doi:10.1038/nn.3419

Pammer L, O'Connor DH, Hires SA, Clack NG, Huber D, Myers EW, Svoboda K. 2013. The mechanical variables underlying object localization along the axis of the whisker. *Journal of Neuroscience* **33**. doi:10.1523/JNEUROSCI.4316-12.2013

Peron S, Chen TW, Svoboda K. 2015. Comprehensive imaging of cortical networks. *Curr Opin Neurobiol*. doi:10.1016/j.conb.2015.03.016

Petersen CCH. 2007. The functional organization of the barrel cortex. *Neuron*. doi:10.1016/j.neuron.2007.09.017

Pi HJ, Hangya B, Kvitsiani D, Sanders JI, Huang ZJ, Kepecs A. 2013. Cortical interneurons that specialize in disinhibitory control. *Nature* **503**. doi:10.1038/nature12676

Pologruto TA, Sabatini BL, Svoboda K. 2003. ScanImage: Flexible software for operating laser scanning microscopes. *Biomed Eng Online* **2**. doi:10.1186/1475-925X-2-13

Reyes-Puerta V, Sun JJ, Kim S, Kilb W, Luhmann HJ. 2015. Laminar and Columnar Structure of Sensory-Evoked Multineuronal Spike Sequences in Adult Rat Barrel Cortex in Vivo. *Cerebral Cortex* **25**. doi:10.1093/cercor/bhu007

Rice FL. 1985. An attempt to find vibrissa-related barrels in the primary somatosensory cortex of the cat. *Neurosci Lett* **53**. doi:10.1016/0304-3940(85)90180-6

Rice FL, Gomez C, Barstow C, Burnet A, Sands P. 1985. AComparative analysis of the development of the primary somatosensory cortex: Interspecies similarities during barrel and laminar development. *Journal of Comparative Neurology* **236**. doi:10.1002/cne.902360405

Roy NC, Bessaih T, Contreras D. 2011. Comprehensive mapping of whisker-evoked responses reveals broad, sharply tuned thalamocortical input to layer 4 of barrel cortex. *J Neurophysiol* **105**. doi:10.1152/jn.00939.2010

Sato TR, Gray NW, Mainen ZF, Svoboda K. 2007. The functional microarchitecture of the mouse barrel cortex. *PLoS Biol* **5**. doi:10.1371/journal.pbio.0050189

Sato TR, Svoboda K. 2010. The functional properties of barrel cortex neurons projecting to the primary motor cortex. *Journal of Neuroscience* **30**. doi:10.1523/JNEUROSCI.3774-09.2010

Shepherd GMG, Svoboda K. 2005. Laminar and columnar organization of ascending excitatory projections to layer 2/3 pyramidal neurons in rat barrel cortex. *Journal of Neuroscience* **25**. doi:10.1523/JNEUROSCI.1173-05.2005

Silberberg G, Markram H. 2007. Disynaptic Inhibition between Neocortical Pyramidal Cells Mediated by Martinotti Cells. *Neuron* **53**. doi:10.1016/j.neuron.2007.02.012

Sosnik R, Haidarliu S, Ahissar E. 2001. Temporal frequency of whisker movement. I. Representations in brain stem and thalamus. *J Neurophysiol* **86**. doi:10.1152/jn.2001.86.1.339

Stachniak TJ, Kastli R, Hanley O, Argunsah AÖ, Van Der Valk EGT, Kanatouris G, Karayannis T. 2021. Postmitotic prox1 expression controls the final specification of cortical VIP interneuron subtypes. *Journal of Neuroscience* **41**. doi:10.1523/JNEUROSCI.1021-21.2021

Stachniak TJ, Sylwestrak EL, Scheiffele P, Hall BJ, Ghosh A. 2019. Elfn1-induced constitutive activation of mglur7 determines frequency-dependent recruitment of somatostatin interneurons. *Journal of Neuroscience* **39**. doi:10.1523/JNEUROSCI.2276-18.2019

Staiger JF, Petersen CCH. 2021. Neuronal circuits in barrel cortex for whisker sensory perception. *Physiol Rev* **101**. doi:10.1152/physrev.00019.2019

Stosiek C, Garaschuk O, Holthoff K, Konnerth A. 2003. In vivo two-photon calcium imaging of neuronal networks. *Proc Natl Acad Sci U S A* **100**. doi:10.1073/pnas.1232232100

Tan Z, Hu H, Huang ZJ, Agmon A. 2008. Robust but delayed thalamocortical activation of dendritic-targeting inhibitory interneurons. *Proc Natl Acad Sci U S A* **105**. doi:10.1073/pnas.0710628105

Taniguchi H, He M, Wu P, Kim S, Paik R, Sugino K, Kvitsani D, Fu Y, Lu J, Lin Y, Miyoshi G, Shima Y, Fishell G, Nelson SB, Huang ZJ. 2011. A Resource of Cre Driver Lines for Genetic Targeting of GABAergic Neurons in Cerebral Cortex. *Neuron* **71**:995–1013. doi:10.1016/j.neuron.2011.07.026

Tanke N, Borst JGG, Houweling AR. 2018. Single-cell stimulation in barrel cortex influences psychophysical detection performance. *Journal of Neuroscience* **38**. doi:10.1523/JNEUROSCI.2155-17.2018

Tomioka NH, Yasuda H, Miyamoto H, Hatayama M, Morimura N, Matsumoto Y, Suzuki T, Odagawa M, Odaka YS, Iwayama Y, Won Um J, Ko J, Inoue Y, Kaneko S, Hirose S, Yamada K, Yoshikawa T, Yamakawa K, Aruga J. 2014. Elfn1 recruits presynaptic mGluR7 in trans and its loss results in seizures. *Nat Commun* **5**. doi:10.1038/ncomms5501

Urban-Ciecko J, Barth AL. 2016. Somatostatin-expressing neurons in cortical networks. *Nat Rev Neurosci* **17**. doi:10.1038/nrn.2016.53

Van Der Bourg A, Yang JW, Reyes-Puerta V, Laurenczy B, Wieckhorst M, Stüttgen MC, Luhmann HJ, Helmchen F. 2017. Layer-Specific Refinement of Sensory Coding in Developing Mouse Barrel Cortex. *Cerebral Cortex* **27**. doi:10.1093/cercor/bhw280

Van Der Loos H, Woolsey TA. 1973. Somatosensory cortex: Structural alterations following early injury to sense organs. *Science (1979)* **179**. doi:10.1126/science.179.4071.395

Vladimirov N, Voigt F, Naert T, Araujo GR, Cai R, Reuss AM, Zhao S, Schmid P, Hildebrand S, Schaettin M, Groos D, Mateos JM, Bethge P, Yamamoto T, Aerne V, Roebroeck A, Ertürk A, Aguzzi A, Ziegler U, Stoeckli ET, Baudis L, Lienkamp SS, Helmchen F. 2023. The Benchtop mesoSPIM: a next-generation open-source light-sheet microscope for large cleared samples. *bioRxiv*.

Voigt FF, Kirschenbaum D, Platonova E, Pagès S, Campbell RAA, Kastli R, Schaettin M, Egolf L, van der Bourg A, Bethge P, Haenraets K, Frézel N, Topilko T, Perin P, Hillier D, Hildebrand S, Schueth A, Roebroeck A, Roska B, Stoeckli ET, Pizzala R, Renier N, Zeilhofer HU, Karayannis T, Ziegler U, Batti L, Holtmaat A, Lüscher C, Aguzzi A, Helmchen F. 2019. The mesoSPIM initiative: open-source light-sheet microscopes for imaging cleared tissue. *Nat Methods* **16**. doi:10.1038/s41592-019-0554-0

Wang HC, LeMessurier AM, Feldman DE. 2022. Tuning instability of non-columnar neurons in the salt-and-pepper whisker map in somatosensory cortex. *Nat Commun* **13**. doi:10.1038/s41467-022-34261-1

Woolsey TA, Welker C, Schwartz RH. 1975. Comparative anatomical studies of the Sml face cortex with special reference to the occurrence of “barrels” in layer IV. *Journal of Comparative Neurology* **164**. doi:10.1002/cne.901640107

Xu H, Jeong HY, Tremblay R, Rudy B. 2013. Neocortical Somatostatin-Expressing GABAergic Interneurons Disinhibit the Thalamorecipient Layer 4. *Neuron* **77**. doi:10.1016/j.neuron.2012.11.004

Yamashita T, Pala A, Pedrido L, Kremer Y, Welker E, Petersen CCH. 2013. Membrane potential dynamics of neocortical projection neurons driving target-specific signals. *Neuron* **80**. doi:10.1016/j.neuron.2013.10.059

Yang JW, Prouvot PH, Reyes-Puerta V, Stüttgen MC, Stroh A, Luhmann HJ. 2017. Optogenetic modulation of a minor fraction of parvalbumin-positive interneurons specifically affects spatiotemporal dynamics of spontaneous and sensory-evoked activity in mouse somatosensory cortex in vivo. *Cerebral Cortex* **27**. doi:10.1093/cercor/bhx261

Young TR, Yamamoto M, Kikuchi SS, Yoshida AC, Abe T, Inoue K, Johansen JP, Benucci A, Yoshimura Y, Shimogori T. 2023. Thalamocortical control of cell-type specificity drives circuits for processing whisker-related information in mouse barrel cortex. *Nat Commun* **14**. doi:10.1038/s41467-023-41749-x

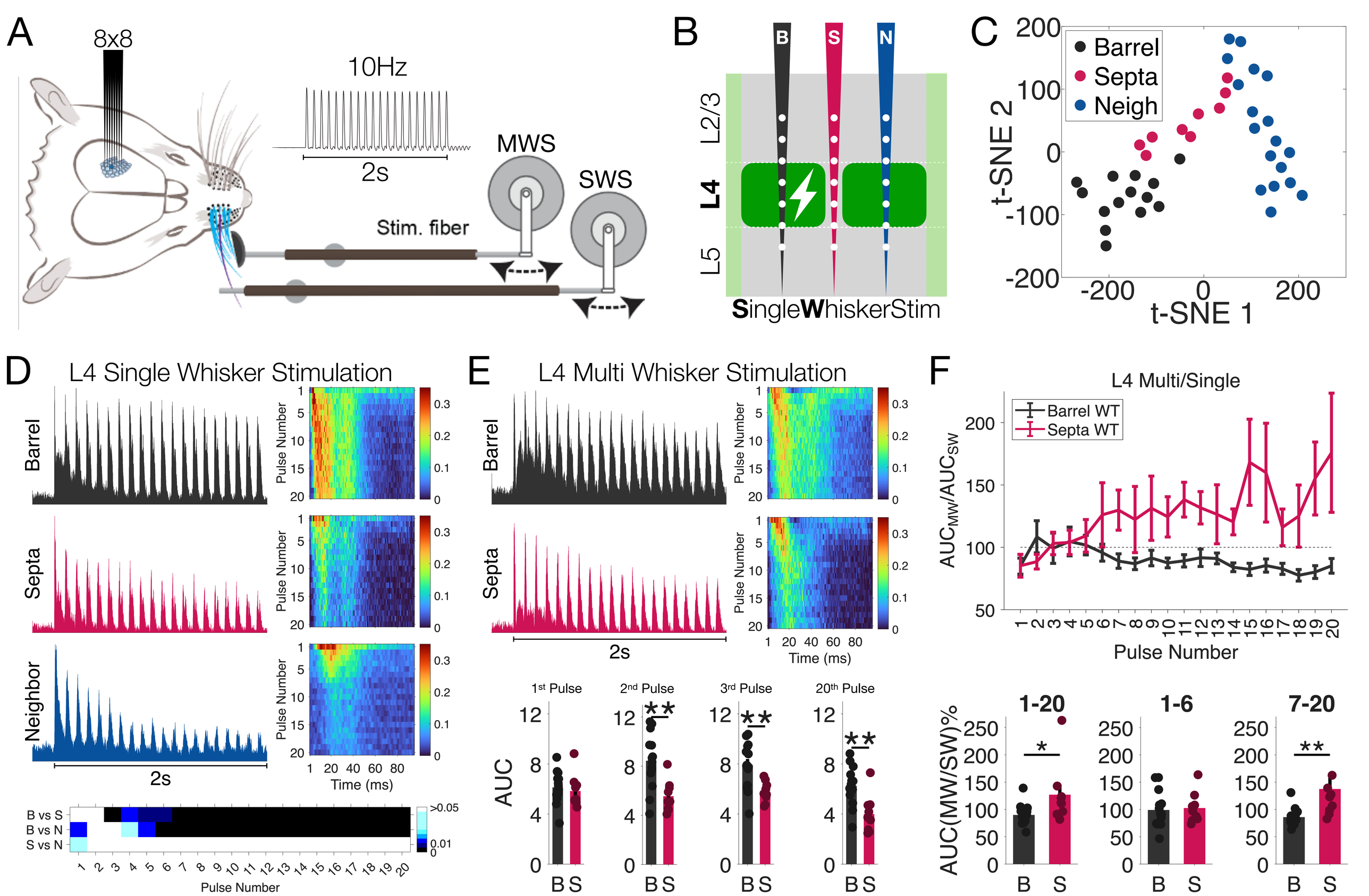
A
8x8
10Hz
2s
MWS
SWS
Stim. fiber
B
B
S
N
L2/3
L4
L5
SingleWhiskerStim
C
Barrel
Septa
Neigh
t-SNE 2
t-SNE 1
D
L4 Single Whisker Stimulation
Barrel
Septa
Neighbor
Pulse Number
Time (ms)
2s
B vs S
B vs N
S vs N
>0.05
0.01
Pulse Number
E
L4 Multi Whisker Stimulation
Barrel
Septa
Pulse Number
Time (ms)
2s
1st Pulse
2nd Pulse
3rd Pulse
20th Pulse
AUC
F
L4 Multi/Single
Barrel WT
Septa WT
AUCMW/AUCSW
Pulse Number
AUC(MW/SW)%
1-20
1-6
7-20

Figure 1

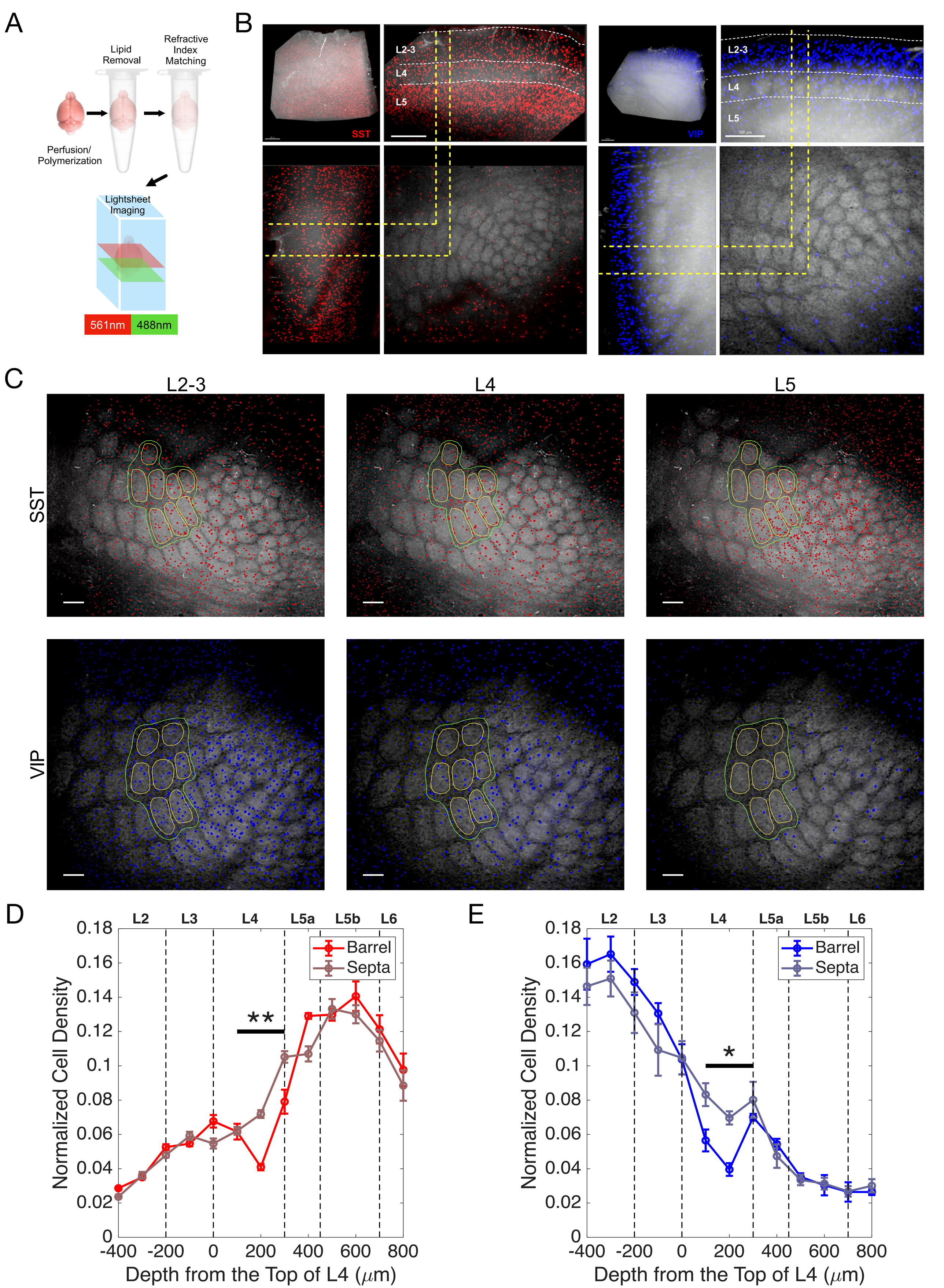
A
Lipid Removal
Refractive Index Matching
Perfusion/ Polymerization
Lightsheet Imaging
561nm
488nm
B
SST
L2-3
L4
L5
VIP
C
L2-3
L4
L5
SST
VIP
D
L2
L3
L4
L5a
L5b
L6
Barrel
Septa
**
Normalized Cell Density
Depth from the Top of L4 (μm)
E
L2
L3
L4
L5a
L5b
L6
Barrel
Septa
*
Normalized Cell Density
Depth from the Top of L4 (μm)

Figure 2

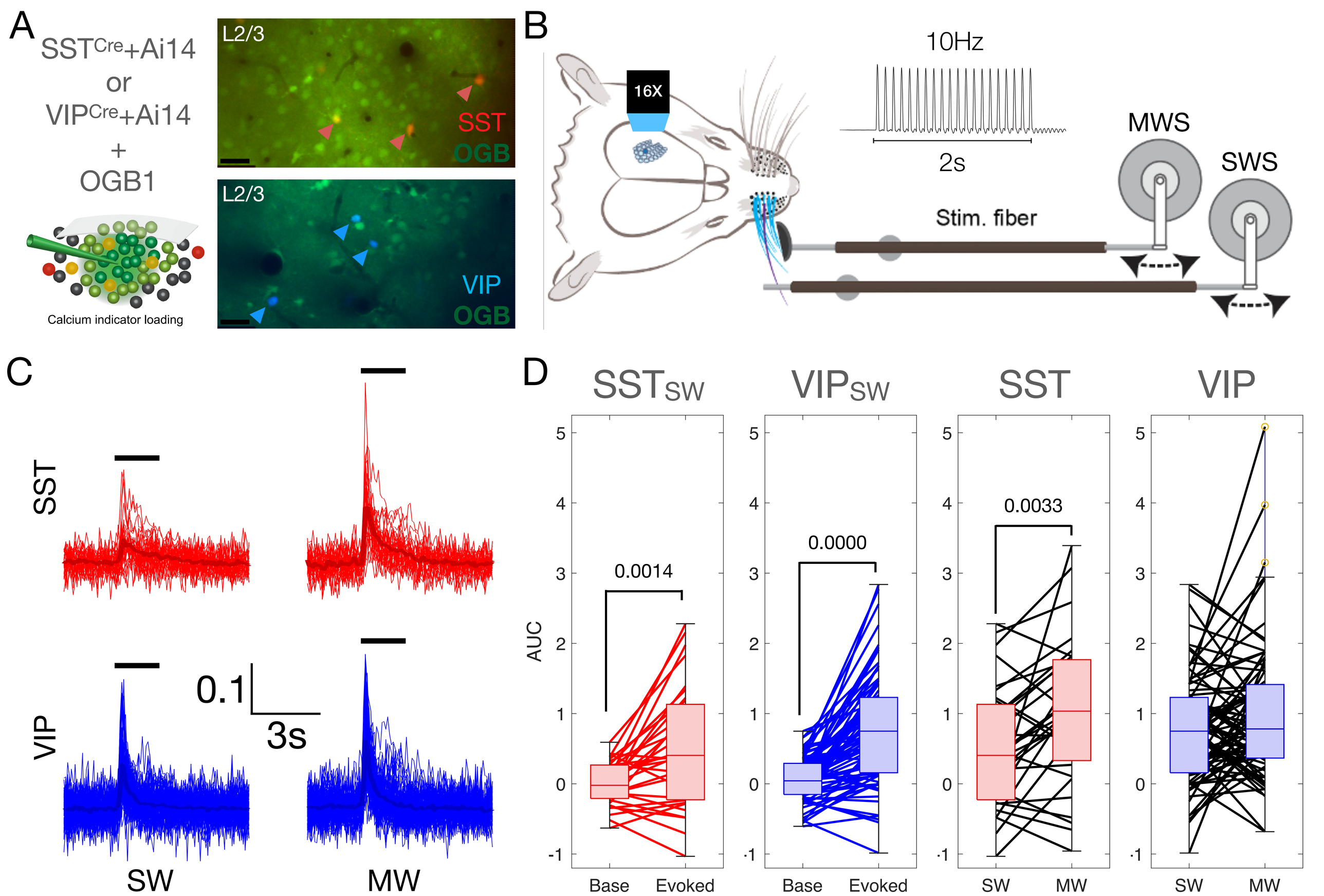
A
SST^Cre+Ai14
or
VIP^Cre+Ai14
+
OGB1
Calcium indicator loading
L2/3
SST
OGB
L2/3
VIP
OGB
B
16X
10Hz
2s
Stim. fiber
MWS
SWS
C
SST
VIP
0.1
3s
SW
MW
D
SST_SW
VIP_SW
SST
VIP
AUC
0.0014
0.0000
0.0033
Base
Evoked
Base
Evoked
SW
MW
SW
MW

Figure 3

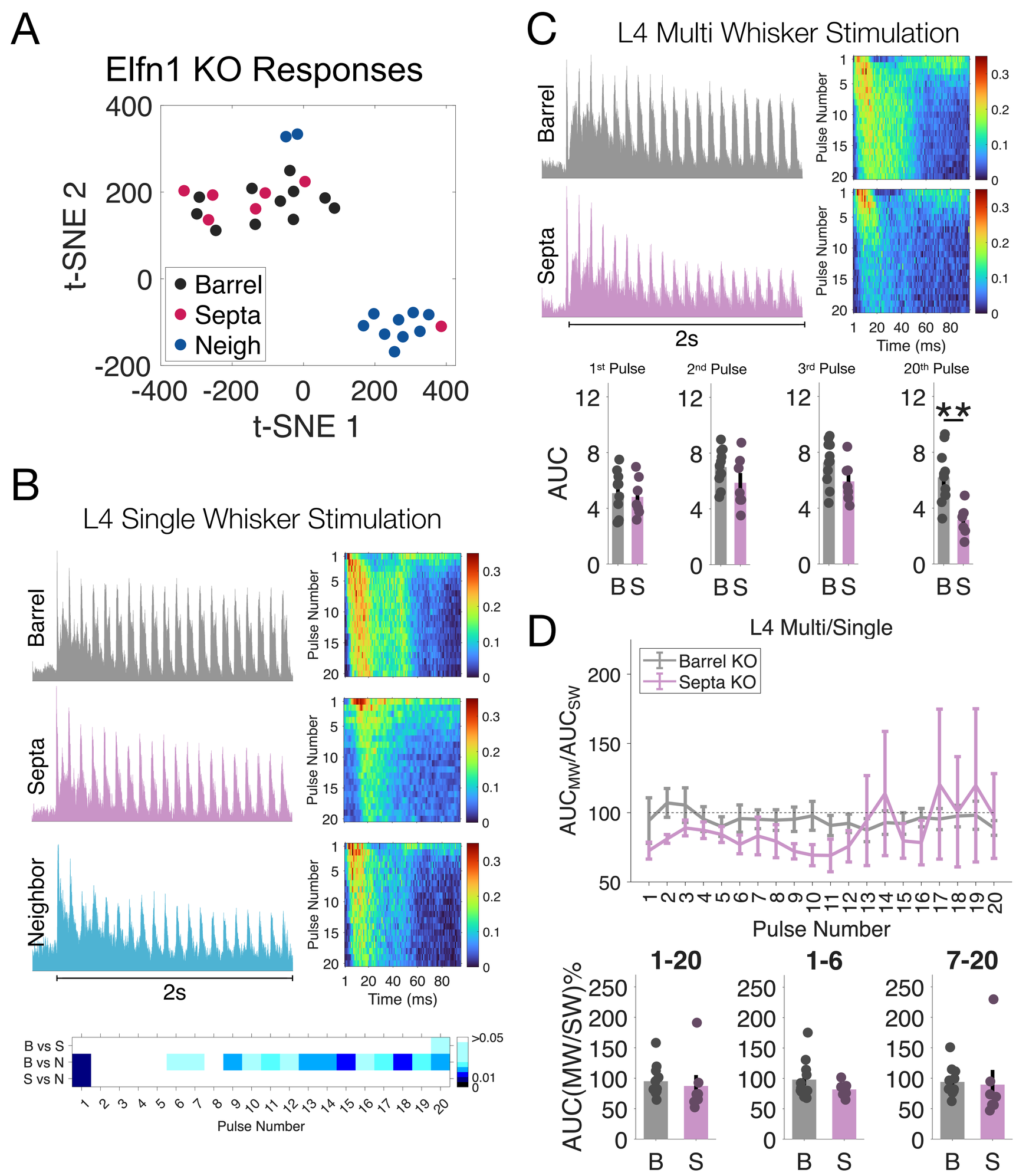
A
Elfn1 KO Responses
t-SNE 2
t-SNE 1
Barrel
Septa
Neigh
B
L4 Single Whisker Stimulation
Barrel
Septa
Neighbor
Pulse Number
Time (ms)
2s
B vs S
B vs N
S vs N
>0.05
0.01
Pulse Number
C
L4 Multi Whisker Stimulation
Barrel
Septa
Pulse Number
Time (ms)
2s
1st Pulse
2nd Pulse
3rd Pulse
20th Pulse
AUC
B S
D
L4 Multi/Single
Barrel KO
Septa KO
AUCMW/AUCSW
Pulse Number
1-20
1-6
7-20
AUC(MW/SW)%
B S

Figure 4

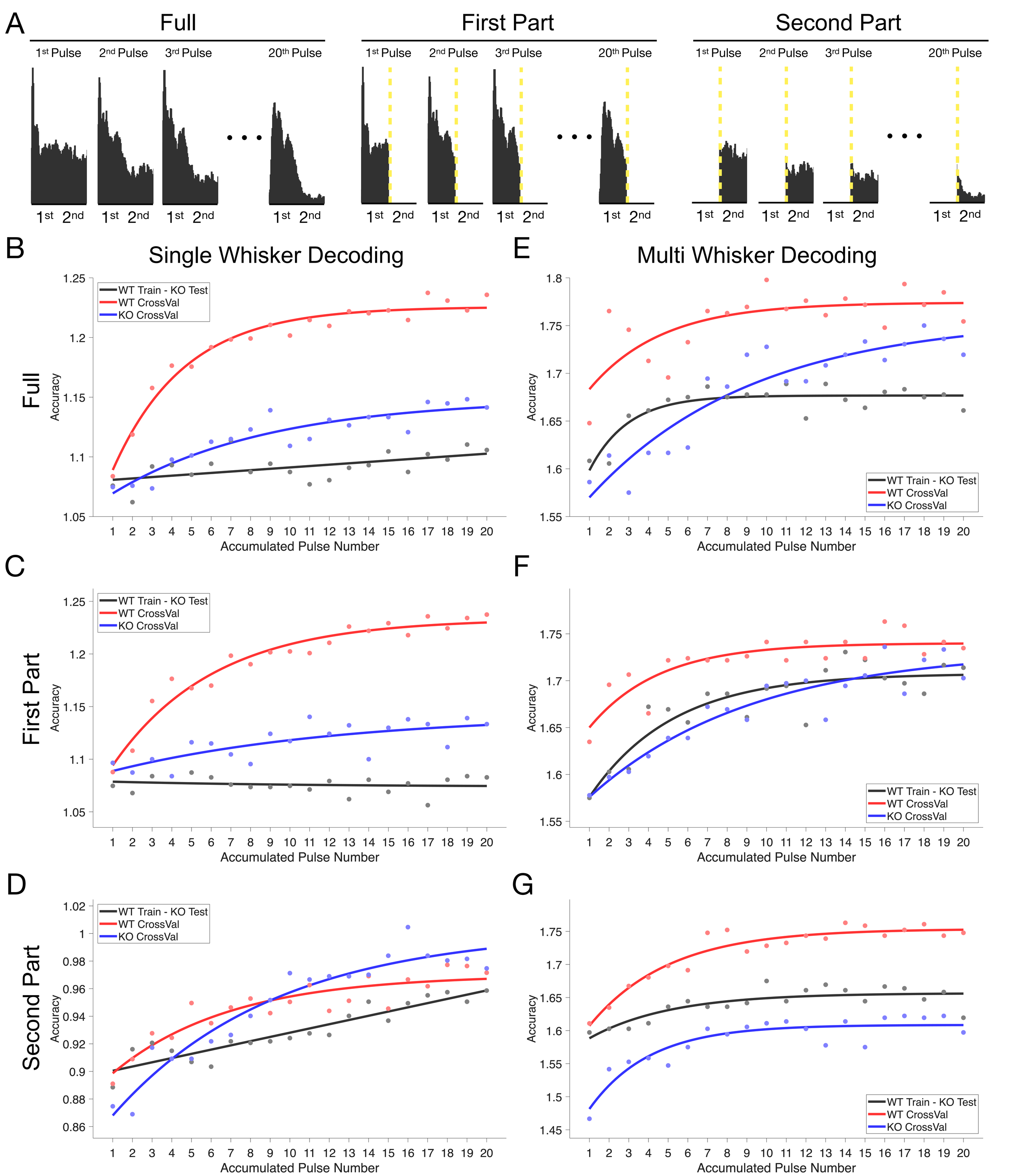
A
Full
First Part
Second Part
1st Pulse
2nd Pulse
3rd Pulse
20th Pulse
1st 2nd
B
C
D
E
F
G
Single Whisker Decoding
Multi Whisker Decoding
Full
First Part
Second Part
Accuracy
Accumulated Pulse Number
WT Train - KO Test
WT CrossVal
KO CrossVal

Figure 5

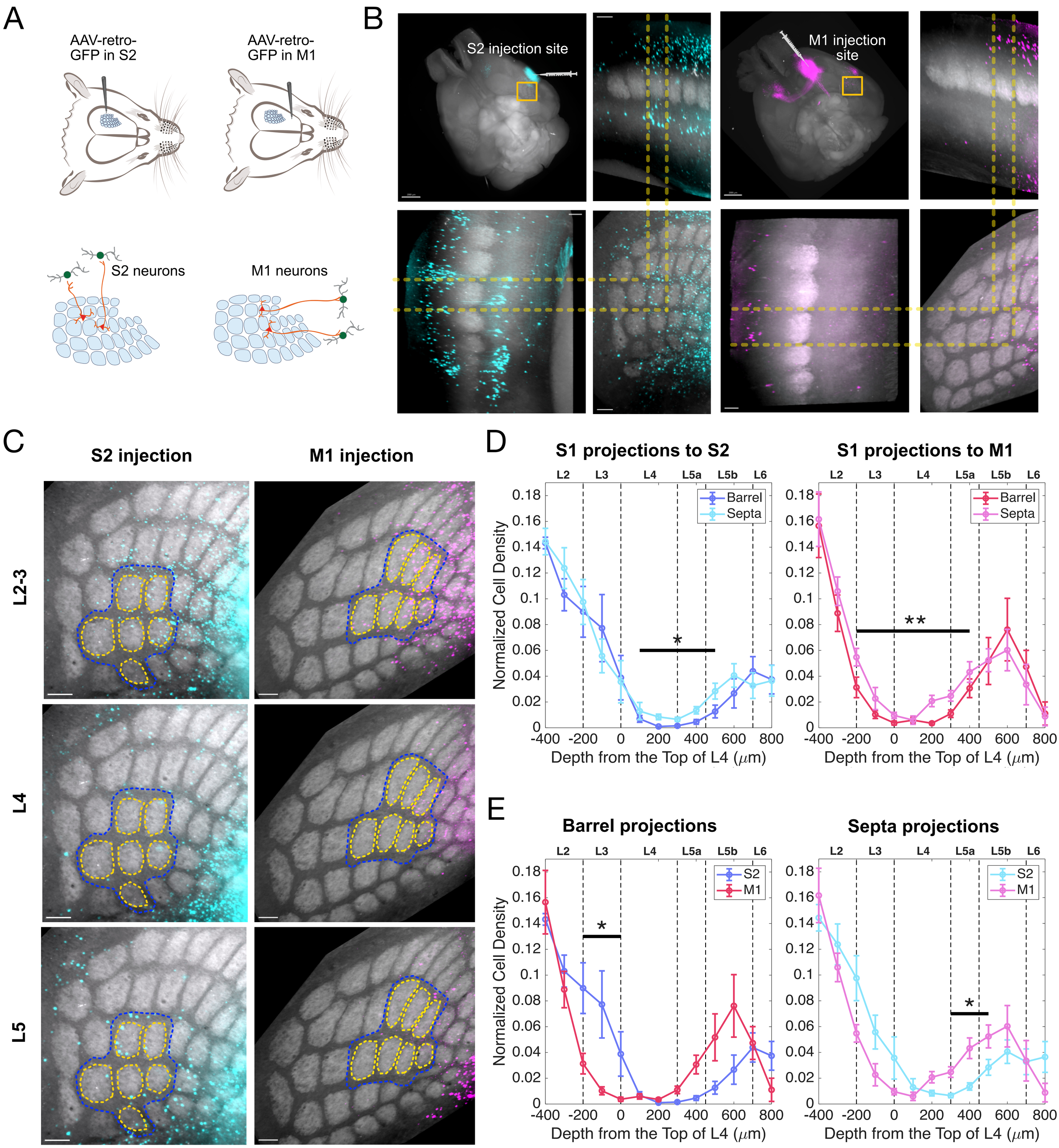
A
AAV-retro-GFP in S2
AAV-retro-GFP in M1
S2 neurons
M1 neurons
B
S2 injection site
M1 injection site
C
S2 injection
M1 injection
L2-3
L4
L5
D
S1 projections to S2
S1 projections to M1
L2
L3
L4
L5a
L5b
L6
Barrel
Septa
Normalized Cell Density
Depth from the Top of L4 (μm)
*
**
E
Barrel projections
Septa projections
S2
M1

Figure 6

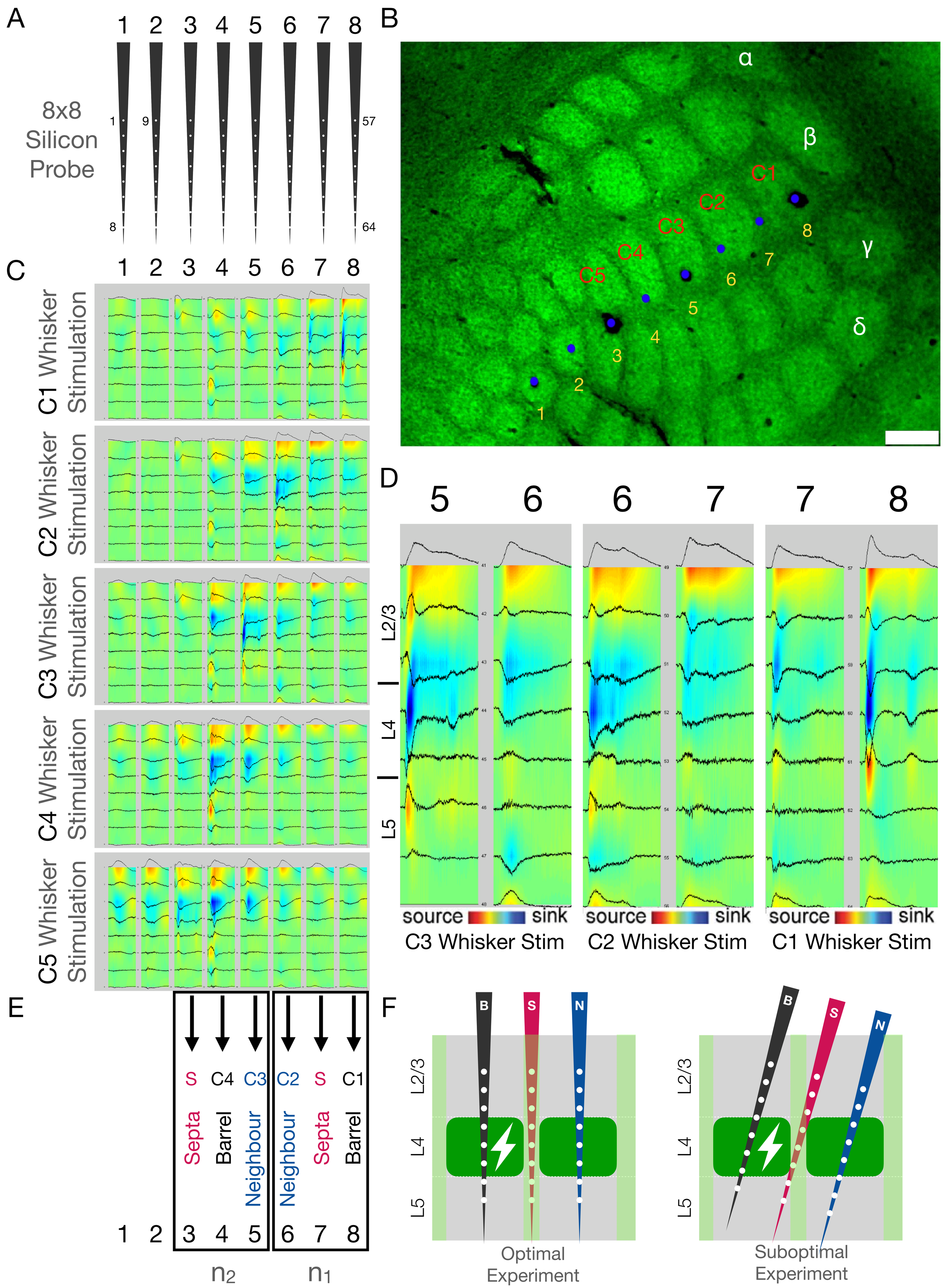


Supplementary Figure 1

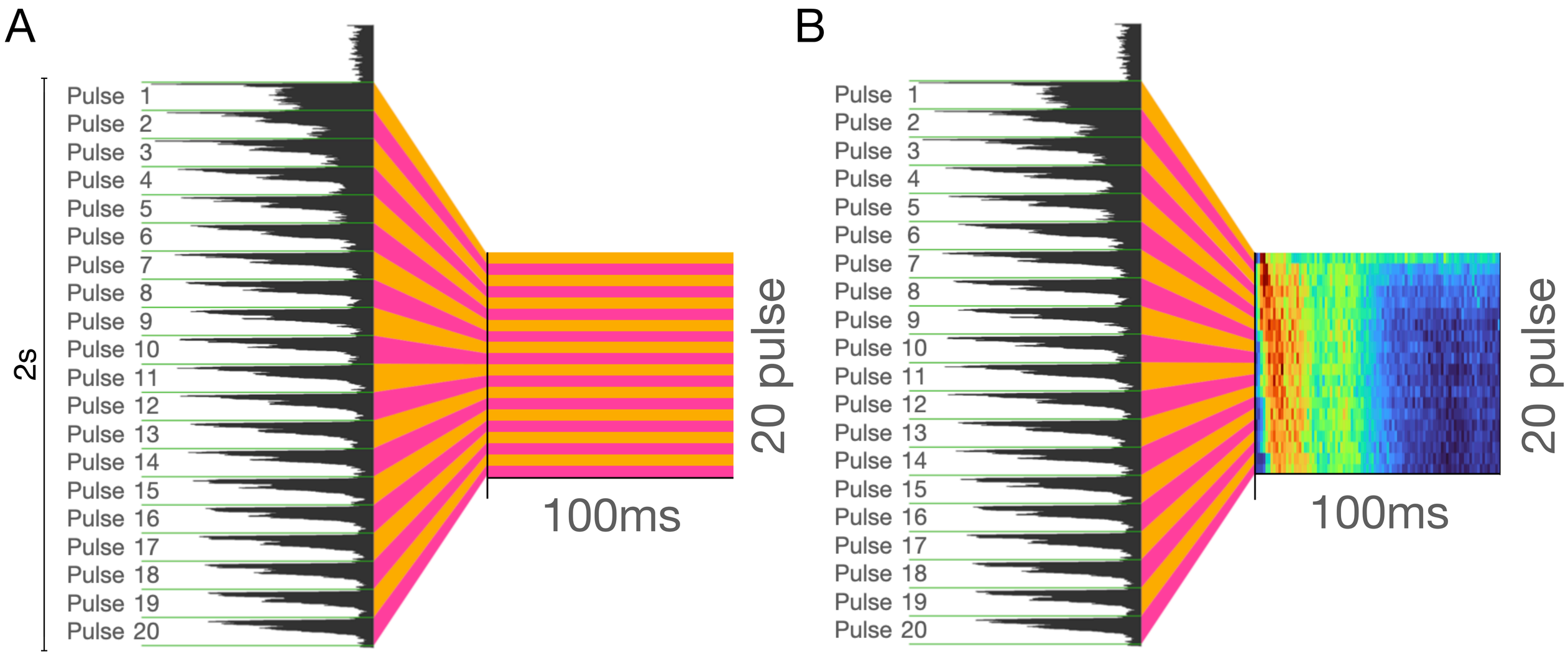


Supplementary Figure 2

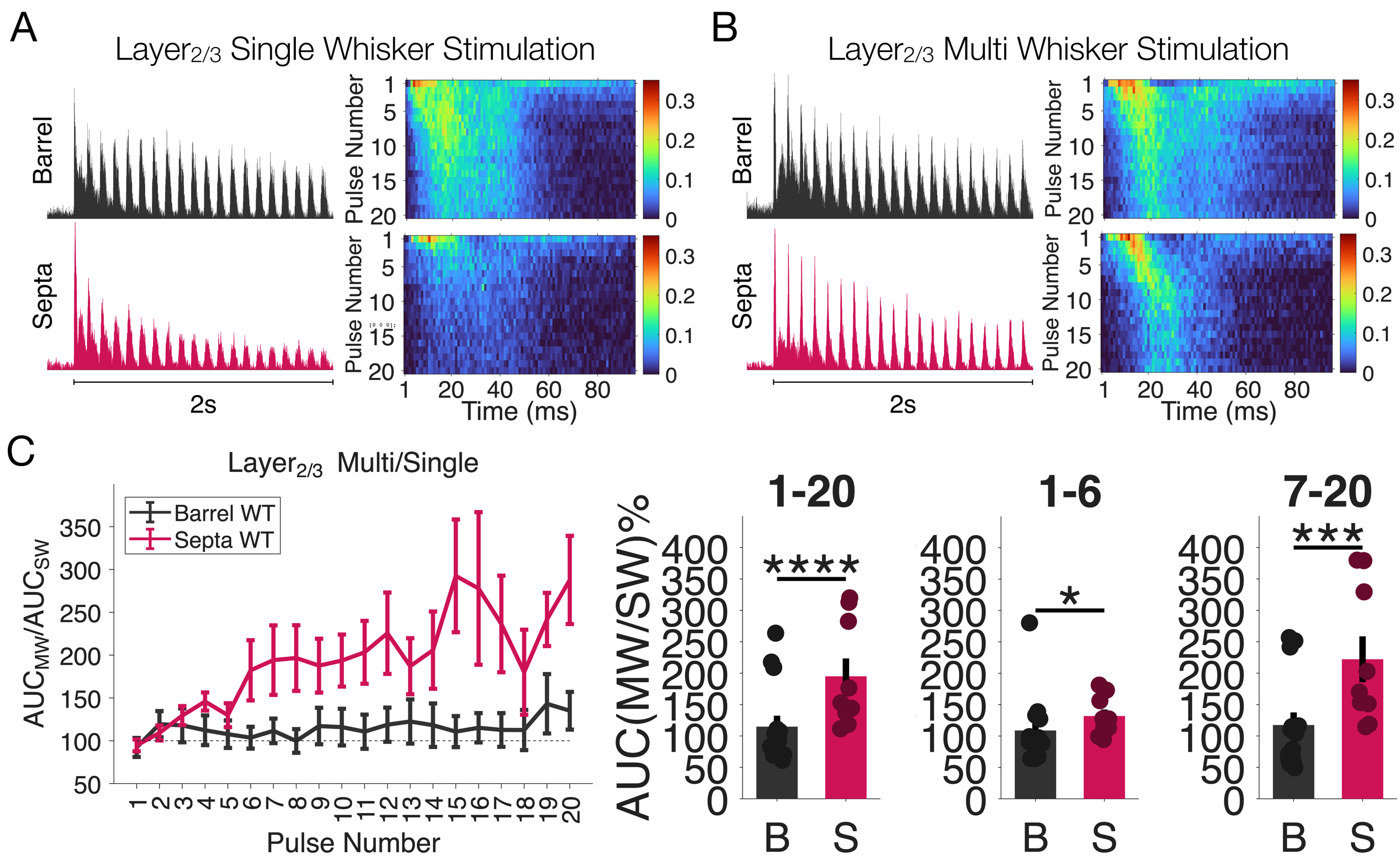


Supplementary Figure 3